

Validation Study for Detection and Quantification of Corrosion in Bridge Barrier Rails

Final Report | December 2018

IOWA STATE UNIVERSITY
Center for Nondestructive Evaluation



IOWA STATE UNIVERSITY
Institute for Transportation

Sponsored by
Federal Highway Administration
Iowa Department of Transportation
(InTrans Project 15-538)

About the Center for Nondestructive Evaluation

The Center for Nondestructive Evaluation (CNDE) is a National Science Foundation Industry/University Cooperative Research Center and is a member of the Institute for Physical Research and Technology at Iowa State University. The Center focuses on the research and development of new theories and techniques for use in quantitative nondestructive evaluation.

Disclaimer Notice

The contents of this report reflect the views of the authors, who are responsible for the facts and the accuracy of the information presented herein. The opinions, findings and conclusions expressed in this publication are those of the authors and not necessarily those of the sponsors.

The sponsors assume no liability for the contents or use of the information contained in this document. This report does not constitute a standard, specification, or regulation.

The sponsors do not endorse products or manufacturers. Trademarks or manufacturers' names appear in this report only because they are considered essential to the objective of the document.

ISU Non-Discrimination Statement

Iowa State University does not discriminate on the basis of race, color, age, ethnicity, religion, national origin, pregnancy, sexual orientation, gender identity, genetic information, sex, marital status, disability, or status as a U.S. veteran. Inquiries regarding non-discrimination policies may be directed to Office of Equal Opportunity, 3410 Beardshear Hall, 515 Morrill Road, Ames, Iowa 50011, Tel. 515-294-7612, Hotline: 515-294-1222, email eooffice@iastate.edu.

Quality Assurance Statement

The Federal Highway Administration (FHWA) provides high-quality information to serve Government, industry, and the public in a manner that promotes public understanding. Standards and policies are used to ensure and maximize the quality, objectivity, utility, and integrity of its information. The FHWA periodically reviews quality issues and adjusts its programs and processes to ensure continuous quality improvement.

Iowa DOT Statements

Federal and state laws prohibit employment and/or public accommodation discrimination on the basis of age, color, creed, disability, gender identity, national origin, pregnancy, race, religion, sex, sexual orientation or veteran's status. If you believe you have been discriminated against, please contact the Iowa Civil Rights Commission at 800-457-4416 or the Iowa Department of Transportation affirmative action officer. If you need accommodations because of a disability to access the Iowa Department of Transportation's services, contact the agency's affirmative action officer at 800-262-0003.

The preparation of this report was financed in part through funds provided by the Iowa Department of Transportation through its "Second Revised Agreement for the Management of Research Conducted by Iowa State University for the Iowa Department of Transportation" and its amendments.

The opinions, findings, and conclusions expressed in this publication are those of the authors and not necessarily those of the Iowa Department of Transportation.

VALIDATION STUDY FOR DETECTION AND QUANTIFICATION OF CORROSION IN BRIDGE BARRIER RAILS

**Final Report
December 2018**

Principal Investigator

David Eisenmann, Associate Scientist
Center for Nondestructive Evaluation
Iowa State University

Authors

David Eisenmann and Frank Margetan

Sponsored by
Iowa Department of Transportation and
Federal Highway Administration

Preparation of this report was financed in part
through funds provided by the Iowa Department of Transportation
through its Research Management Agreement with the
Institute for Transportation
(InTrans Project 15-538)

A report from
Institute for Transportation
Iowa State University
2711 South Loop Drive, Suite 4700
Ames, IA 50010-8664
Phone: 515-294-8103 / Fax: 515-294-0467
www.intrans.iastate.edu

TABLE OF CONTENTS

ACKNOWLEDGMENTS	ix
EXECUTIVE SUMMARY	xi
Ground Penetrating Radar.....	xi
Magnetic Flux Leakage Detection	xii
BACKGROUND	1
Review and Introduction.....	1
Research Objectives.....	3
Project Scope	8
SUMMARY OF PRIOR WORK.....	9
Problem Statement	9
Results from Prior Work.....	9
TEST AND EVALUATION METHODOLOGIES	14
Discussion of Methodologies.....	14
Evaluation of GPR Methods	14
Evaluation of Electromagnetic Methods.....	17
TEST AND EVALUATION OF RESULTS	18
Ground Penetrating Radar Laboratory Results	18
Ground Penetrating Bridge Results	40
Electromagnetic Testing	50
Electromagnetic Bridge Results.....	61
CONCLUSIONS AND RECOMMENDATIONS	62
FUTURE WORK.....	63
REFERENCES	65

LIST OF FIGURES

Figure 1. Control samples constructed for Phase I	1
Figure 2. Location of IA 210 bridge over I-35 in southwest Story County, Iowa.....	2
Figure 3. Model-generated GPR B-scans containing responses from an air/solid interface (front-wall) and a small embedded reflector simulating reinforcing steel.....	4
Figure 4. Assumed simplified geometry for thinned reinforcing steel	5
Figure 5. Measurement setups investigated for assessing concrete property variations within structures: (a) and (b) pulse/echo setups requiring only one GPR antenna and (c) pitch/catch setup requiring two antennas.....	6
Figure 6. Probe design that combined magnetic reluctance and MFL measurements for inspecting reinforcing steel in concrete structures	7
Figure 7. Portable GSSI ground penetrating radar equipment employing a single 1600 MHz antenna	14
Figure 8. GPR pulse/echo inspection of reinforcing steel, and analogy with ultrasonic inspection	15
Figure 9. (a) Scan of GPR antenna across three abutting test blocks each containing one embedded reinforcing steel bar, (b) resulting B-scan image, (c) and (d) why reinforcing steel B-scan responses have a characteristic hyperbola shape, and (e) GPR A-scan plot of output voltage versus time for antenna position indicated by vertical black line in panel (d).....	16
Figure 10. (a) Some of the many possible setups for normal-incidence attenuation measurements and (b) general form of the model expression used in attenuation deduction	18
Figure 11. (a) Pitch/catch setup for measuring beam-spread effects in air, (b) typical raw GPR signal before and after windowing, (c) spectral magnitudes of measured signals for different antenna separation distances ranging from 6 to 42.5 in., (d) measured and fitted spectral magnitudes at 1.6 GHz, and (e) dependence of the parameter Δ on frequency	20
Figure 12. (a) Equivalence (under paraxial approximations) between pulse/echo and pitch/catch beam-spread measurement setups for two identical antennas, (b) pulse/echo signal reflected from a metal plate in air before and after subtraction of the direct-coupled signal, (c) comparison of (broadband) beam-spread effects for pulse/echo and pitch/catch measurements, and (d) handling of beam-spread corrections in concrete	22
Figure 13. Attenuation measurements on concrete patio blocks: (a) setup phase, (b) raw GPR signals for one case (3-in. gap), (c) arrival time graph used to deduce EM wave speed in concrete for one case (3-in. gap), (d) amplitude fall rate for one case (3-in. gap), (e) amplitude loss in decibels relative to 0-block signal, and (f) attenuation versus frequency as deduced from spectral magnitudes of windowed signals.....	23
Figure 14. Simple measurement setup used to quantify strengths of spurious GPR signals associated with travel paths that bypass blocks under study.....	25

Figure 15. (a) Setups for attenuation measurements on cast concrete blocks (24-in. antenna separation for P/C), (b) cast block with metal plate in place for enhanced back-wall (EBW) echo acquisition, (c) raw GPR signals for setup P/E-1 using 2-in. cast block, and (d) resulting front wall (FW) and EBW echoes (prior to windowing) deduced by signal subtraction.....	26
Figure 16. (a) Spectral amplitudes for some of the signals involved in determining attenuation of 2-in. and 4-in. thick cast blocks and (b) deduced attenuation-vs-frequency curves for cast blocks using various methods.....	27
Figure 17. (a) Coordinate system centered on the GPR antenna and (b) setups used for measurements of reinforcing steel in air.....	28
Figure 18. Examples of lab setups and of background signal subtraction for a long reinforcing steel bar containing a 1-in. gap.....	30
Figure 19. Effect of varying the reinforcing steel depth, Z	31
Figure 20. Effect of varying the reinforcing steel length, L	31
Figure 21. Effect of varying the reinforcing steel rotation angle θ	32
Figure 22. Effect of varying the reinforcing steel tilt angle ϕ	33
Figure 23. Effect of varying the reinforcing steel gap length G	33
Figure 24. For a 1-in. reinforcing steel gap, effect of varying the gap location C	34
Figure 25. Reinforcing steel-in-concrete-phantom measurement details: (a) laboratory setup, (b) and (c) reinforcing steel in wooden frame before and after moist sand added, and (d) and (e) reinforcing steel targets used to simulate loss of metal due to corrosion.....	35
Figure 26. Effect of reinforcing steel rotation: (a) measurement setup, (b) representative GPR signals as measured, (c) reinforcing steel signals after background subtraction, and (d) dependence of peak-to-peak reinforcing steel amplitude on rotation angle, normalized to be unity at zero angle.....	37
Figure 27. Effect of varying the gap location C for a 1-in. reinforcing steel gap.....	38
Figure 28. Effect of varying the offset distance C for a 1-in. long, 50%-thinned region.....	39
Figure 29. Identification of regions of interest on the bridge deck.....	40
Figure 30. Data collection illustrating the spacer used in collection of the reference data.....	41
Figure 31. Example of B-scans and amplitude data take from a section of the bridge.....	41
Figure 32. Compilation of data collected in 2012 from all inspected sections.....	42
Figure 33. New antenna positions for data collection.....	43
Figure 34. Gap shown in the bridge deck near an inspection site.....	43
Figure 35. Amount of concrete removed during initial repair efforts.....	44
Figure 36. Configuration of material used to elevate the antenna to mimic the 2012 inspection location.....	44
Figure 37. Example of data collected on three different levels.....	45
Figure 38. Same data with SAFT performed.....	45
Figure 39. Combined data from one section showing both field dates.....	46
Figure 40. Data collection from June 2012.....	47
Figure 41. Data collection from December 2016.....	47
Figure 42. Data collection from June 2017.....	48
Figure 43. Reinforcing steel taken from IA 210 bridge after demolition of part of the bridge.....	49
Figure 44. Material loss due to corrosion from reinforcing steel in Figure 5.....	50

Figure 45. Reconstructed MFL system.....	51
Figure 46. (a) Bare #4 reinforcing steel samples and (b) mockup samples consisting of either #4 or epoxy-coated #6 reinforcing steel bars.....	51
Figure 47. (a) Experimental setup for performing MFL scans on bare reinforcing steels and mockup samples, (b) close-up of MFL sensor probe consisting of an electromagnet to apply magnetizing field and two GMR sensors to detect the vertical component of leakage field at the pole-piece of the electromagnet, and (c) nominal output of the GMR sensors versus magnetic field.....	53
Figure 48. Difference in material loss between 25% (left) and 50% (right) material removal with a 2-in. standoff distance.....	54
Figure 49. Difference in material loss between 25% (left) and 50% (right) material removal with a 3-in. standoff distance.....	55
Figure 50. A 10° tilt combined with a standoff of 2 in., and material removal of 25% (left) and 50% (right).....	55
Figure 51. A 10° tilt combined with a standoff of 3 in., and material removal of 25% (left) and 50% (right).....	55
Figure 52. An increase of 5 mm in the Z direction during scanning, and material removal of 25% (left) and 50% (right).....	56
Figure 53. An increase of 5 mm in step in the X direction during scanning, and material removal of 25% (left) and 50% (right).....	56
Figure 54. An increased step with 25% material loss (left) and an increased step with 50% material loss (right).....	57
Figure 55. A change in step and in tilt angle for 25% material loss (left) and 50% material loss (right).....	57
Figure 56. Concrete sample with a step increase in the Z direction with 0° tilt, and material removal of 25% (left) and 50% (right).....	58
Figure 57. Concrete sample with a step increase in the Z direction with 10° tilt, and material removal of 25% (left) and 50% (right).....	58
Figure 58. Concrete sample with a step increase in the X direction with 0° tilt, and material removal of 25% (left) and 50% (right).....	59
Figure 59. Concrete sample with a step increase in the Z direction with 10° tilt, and material removal of 25% (left) and 50% (right).....	59
Figure 60. A 10 mm step for the X and Z directions with 0° tilt for material removal of 25% (left) and 50% (right).....	60
Figure 61. A 10 mm step for the X and Z directions with 10° tilt for material removal of 25% (left) and 50% (right).....	60

LIST OF TABLES

Table 1. Comparison of MFL and GPR prediction of damage.....	13
Table 2. Dimensions of the artificial defects in bare #4 reinforcing steel bars shown in Figure 46a.....	52
Table 3. List of mockup concrete samples (Figure 46b) used in the Stage 2 study.....	52

ACKNOWLEDGMENTS

The authors would also like to thank the Iowa Department of Transportation (DOT), which used Federal Highway Administration (FHWA) state planning and research funds as part of their funding.

EXECUTIVE SUMMARY

This program set out to validate three nondestructive evaluation methods: ground penetrating radar (GPR), magnetic flux leakage (MFL), and radiography, to determine the amount of material loss from a bridge inspected in an earlier phase of the research. During the early part of the program, it was decided by mutual agreement between the researchers and the Iowa Department of Transportation (DOT) that the use of radiography would be eliminated from the project due to the cost and potential public relations issues related to the use of limited radiation over an interstate highway. Proceeding forward, the project evaluated the feasibility of two technologies, GPR and a MFL approach using a giant magneto resistive sensor for the detection and quantification of corrosion in embedded reinforcement bars.

Two sets of control samples were used in the project: a set of bare reinforcing steel samples with 0%, 25%, and 50% material loss, and a set of controlled samples containing a pristine reinforcing bar and bars with 25% and 50% section reductions that were embedded in concrete at a 2.5-in. depth. The controlled samples were used to further refine the data collection and processes and to develop a better understanding of the effects on the data collected. The techniques were also used in a limited field trial on the IA 210 Bridge that serves as an overpass for I-35 in Story County, Iowa. Primary conclusions for each of the methods are provided below.

Ground Penetrating Radar

GPR signals from concrete structures are affected by several phenomenon, including: (1) transmission and reflection coefficients at interfaces, (2) the radiation patterns of the antenna(s) being used, and (3) the material properties of concrete and any embedded objects. The different schemes for determining the electromagnetic (EM) attenuation of concrete from measured signals obtained using commercially-available GPR equipment were investigated. Procedures commonly used in ultrasonic inspections were adapted, where comparisons are made of the relative strengths of two or more signals with different travel paths through the material of interest. After correcting for beam spread (i.e., diffraction), interface phenomena, and equipment amplification settings, any remaining signal differences were assumed to be due to attenuation, thus allowing the attenuation coefficient (e.g., decibels [dB] of loss per inch of travel) to be estimated.

Many factors can contribute to the strength of the reflected radar echo seen from a given section of reinforcing steel, including the reinforcing steel's length, its distance from and tilt angle relative to the antenna, and the location and size of the metal loss region. These geometric effects were systematically investigated.

Measurements were made of reflected signals where only an air layer separated the antenna from the reinforcing steel. Using standard 0.5-in. diameter reinforcing steel bars, the GPR signal was systematically studied as a function of the length of the reinforcing steel, the stand-off distance from the antenna, the reinforcing steel tilt angle, and the size of the metal loss region. The metal loss region was simulated by taking two parallel and abutting reinforcing steel lengths and pulling them apart to introduce a small gap between them. The "in air" measurements indicated

that that GPR signal amplitude was quite sensitive to material loss, but care was taken to compensate for effects due to reinforcing steel depth and orientation. Efforts were made to extend the study to reinforcing steel embedded in concrete by developing a material to act as a “phantom” material (having GPR properties similar to concrete) that was sandwiched between two concrete blocks. The reinforcing steel was then inserted into the powder layer and its position and orientation was altered at will.

Magnetic Flux Leakage Detection

A MFL sensor was reconstructed from a previous design using giant magnetoresistance (GMR) sensors. Laboratory tests showed a detectable difference in the signal response with material loss or tilt angle, which indicated the potential ability to quantify corrosion damage in reinforcing steel. Measurements were sensitive to the interference from other metal objects that were in close proximity to the GMR sensors. The application of this technique was very sensitive to both the surrounding material and the environment during the inspection time. The conditions present during the 2016 data collection caused issues with the equipment’s operation. The physical condition of the bridge during the 2017 data collection period prohibited the use of the MFL system, given the lack of a uniform bridge deck on which to place the GMR sensors.

An unfortunate lack of communication between the contractors and the research team resulted in the destruction of the initially inspected reinforcing steel, from both the 2012 phase of the program and the more recent data collection periods. With the acquisition of reinforcing steel bars from the north side of the same bridge, an assessment was made of the amount of corrosion that unprotected reinforcing steel can experience. In the Future Works section of this report, a short-term validation study is proposed.

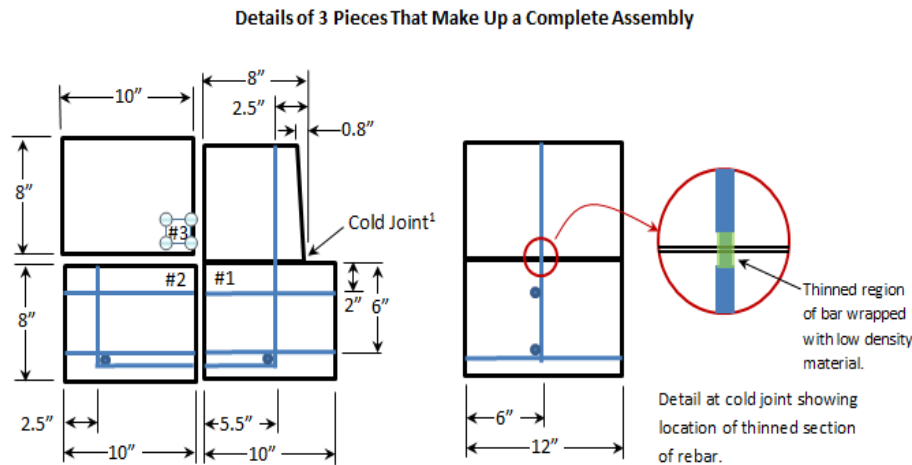
BACKGROUND

Review and Introduction

Locating the position of reinforcing steel bars in concrete structures is a routine procedure with a number of commercial-off-the-shelf (COTS) tools available such as ground penetrating radar (GPR), radiography, and electromagnetic devices (such as the reinforcing rebaroscope from James Instruments Inc.). While instrumentation and inspection service providers are available to support position verification, the ability to provide quantitative information about the condition of embedded reinforcing bars and other anchoring components, such as anchor bolts, is lacking.

Without quantitative information regarding the extent of degradation, condition-based decisions regarding the repair or replacement of reinforced structures are not possible. The purpose of the initial phase of this project (Phase I) was to determine the feasibility of generating quantitative data showing the extent of material loss and to provide recommendations on the fieldability of these approaches. The results of Phase I determined that this sort of data generation is feasible.

In the initial phase, there were three technologies evaluated: x-ray radiation, GPR, and a magnetic flux leakage (MFL) approach using a giant magnetoresistance (GMR) sensor. A set of controlled samples (Figure 1) containing pristine reinforcing steel with and without epoxy, and reinforcing steel with 25% and 50% section reduction, were embedded in concrete at a depth of 2.5 in. from the sample surface.



- Notes: 1 – Cold joint could be simulated using a thin piece of plastic to separate the two pieces.
2 – Embed bent rebar for handles for lifting on sides of specimens.

Figure 1. Control samples constructed for Phase I

The controlled samples were used to develop each of the three methods. Two of the techniques, GPR and MFL, were also used in a limited field test on the IA 210 Bridge over I-35 in southwest Story County, Iowa (see Figure 2).

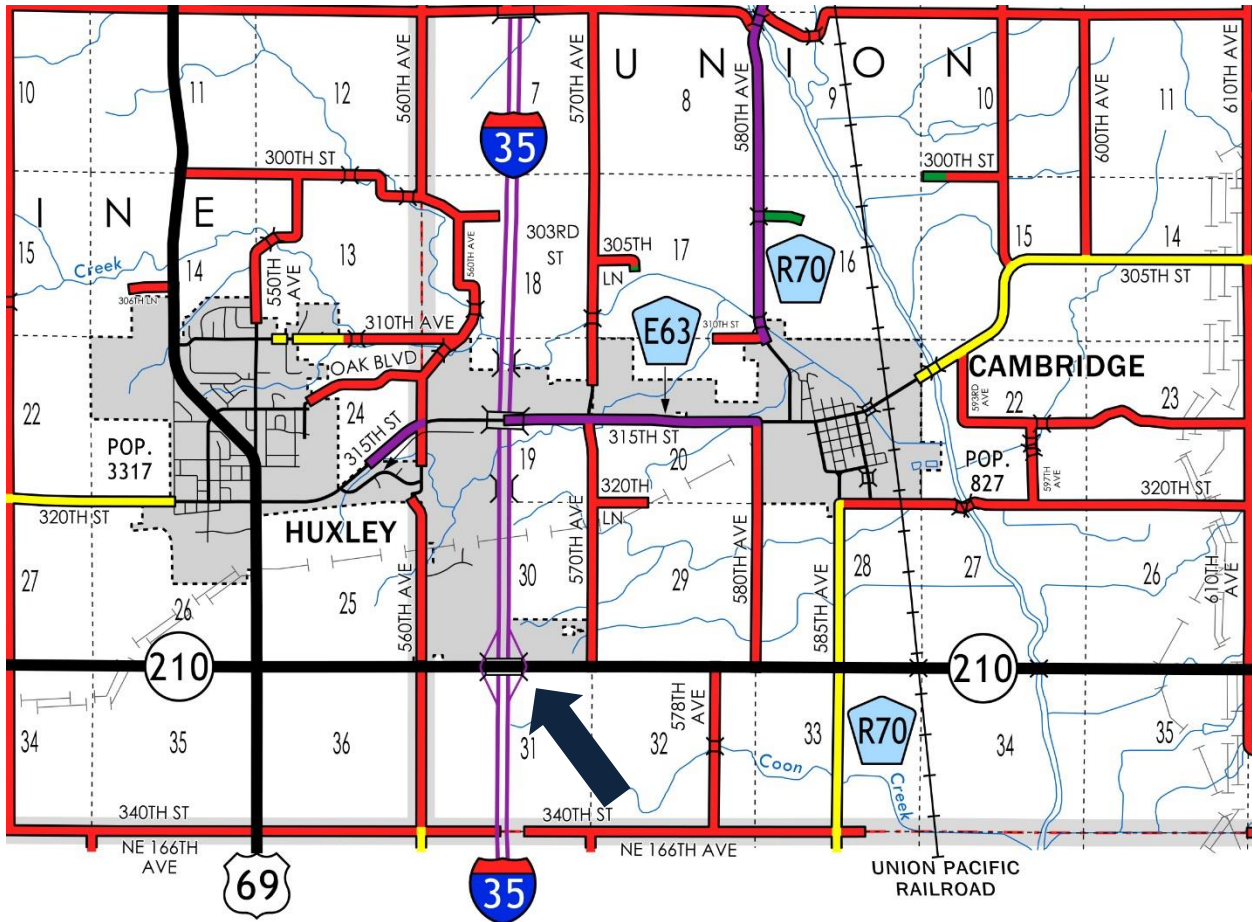


Figure 2. Location of IA 210 Bridge over I-35 in southwest Story County, Iowa

Primary conclusions for each of the three methods were as follows:

- Radiographic inspection provides a projection image of the position and condition of the reinforcing steel. Proper selection of the source is needed to ensure penetration of the x-ray energy through typical thicknesses of concrete. Several detector options are also available including film and digital detectors. Researchers have been hesitant to use radiography because of cost and health safety concerns (e.g., exclusion zones are needed to prevent inadvertent radiation exposure to humans). However, modern digital x-ray detectors reduce the exposure time and use less radiation, thus increasing the benefit-to-cost ratio for this method. Further improvements could result from the use of backscatter x-ray methods, which is a topic recommended for future study. The actual visual evidence of the reinforcing steel condition could lead to more effective decision making regarding bridge maintenance actions and ensure that scarce infrastructure resources are used where they are needed most.
- Use of GPR for locating reinforcing steel in concrete is well-documented. In this project, techniques were developed to detect corrosion damage using laboratory samples and then applied to the inspection of 88 reinforcing bars on the IA 210 Bridge, moving this method beyond mere location of reinforcing bars to condition assessment. The method compared the

response in a known undamaged region to the response close to the potential damage areas near the cold joint. Of the 88 reinforcing bars inspected, 11 were found to be anomalous. Agreement was found between the GPR and MFL results for those locations that were inspected using both methods.

- A MFL sensor was designed and fabricated using GMR sensors. Laboratory tests showed a monotonic decrease in signal response with material loss. This indicated the ability to quantify corrosion damage in standalone reinforcing steel. Because interference can occur when reinforcing bars are in close proximity, application of this technique required independent knowledge of the location of the reinforcing bars. Future sensor designs could combine an eddy current (EC) sensor with the MFL measurement to address this issue. The sensor was also used to inspect 18 reinforcing bar locations on the IA 210 Bridge over I-35. Of the 18 locations, 13 showed a stronger off-deck response than the measurements near the cold joint, indicating suspect conditions.

Each of the methods considered in this research project provided useful and complementary information. GPR offered a rapid approach to identifying reinforcing steel that had anomalous responses. The MFL technique supplied similar detection responses but could be better optimized to provide a more quantitative correlation to the actual reinforcing steel condition. In future inspections employing the technologies from Phase I, either GPR or MFL methods could be used to identify areas of concern on a barrier rail. Radiography could then be used to give a projection image of the actual condition at those points, providing the final guidance needed to plan bridge maintenance actions.

Research Objectives

In the initial proposal for Phase II, all three methods of nondestructive evaluation used in Phase I were considered for work in Phase II. However, after careful consideration it was decided by both the Iowa Department of Transportation (DOT) and Center for Nondestructive Evaluation (CNDE) that the use of radiography would not be employed in this second phase of work. Below are the studies that were included in the scope of Phase II of the project.

New GPR Studies

The GPR research had two major tasks:

1. At a highway bridge scheduled for barrier rail replacement, GPR reinforcing steel signatures were measured prior to demolition. These signatures were compared with reinforcing steel corrosion damage seen visually after demolition in an attempt to correlate the two.
2. Laboratory models of GPR inspections were developed. The models were used to estimate the likely sensitivity and reliability of GPR inspections for detecting the thinning of reinforcing steel due to corrosion.

Field Measurements and Analysis

The initial task made use of the GPR data acquisition method used in the earlier bridge study. GPR B-scans of barrier rail sections were made in two ways: (1) with the antenna flush to the barrier rail near the cold joint and (2) with the antenna flush to the barrier rail and elevated approximately 1.5 in. above the cold joint. For each reinforcing steel response, a reflected amplitude and an arrival time was extracted from the data. The analysis of the reinforcing steel response made use of both the raw B-scan data and data processed using synthetic aperture focusing techniques (SAFT). Note that the radiation field from the GPR antenna used in the research was not focused. If it were focused at a particular depth, reflected signals from objects at that depth would be enhanced. SAFT provides a way to improve image quality to that comparable for a focused antenna by combining measurements made at a sequence of lateral positions. This method is described by Eisenmann et al. (2013).

Figure 3 demonstrates the results of applying SAFT to a model-generated B-scan image. Figure 3a shows the raw B-scan, and Figure 3b shows the B-scan after the SAFT processing.

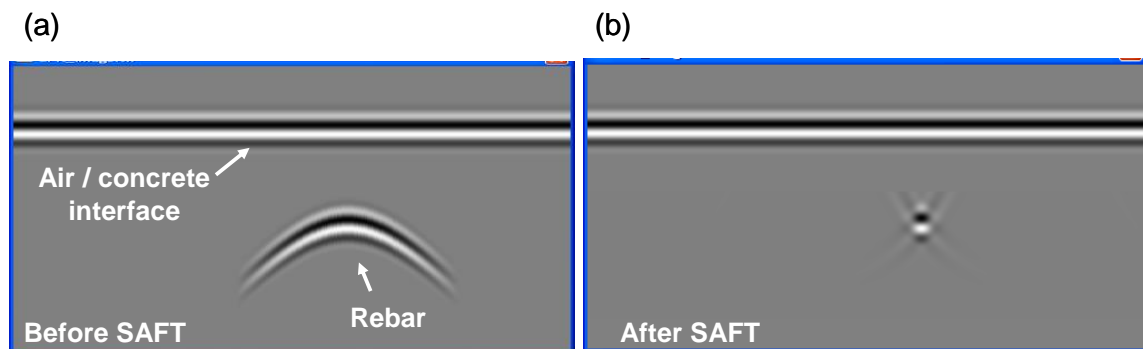


Figure 3. Model-generated GPR B-scans containing responses from an air/solid interface (front-wall) and a small embedded reflector simulating reinforcing steel

After SAFT processing the “response hyperbola” for the embedded reflector was greatly compressed in the horizontal direction, resulting in a higher-contrast peak response and a more readily identified reflector location. In the earlier bridge study, SAFT was not used, so peak amplitude and arrival time values for each reinforcing steel bar were simply determined from the high-amplitude pixel in the raw GPR B-scan. In the Phase II work, peak amplitude and arrival time were extracted from both the raw and SAFT versions of the B-scan. Because SAFT effectively concentrates the response hyperbola, many different antenna positions contribute to the peak amplitude that is seen. This provided a more reliable estimate of both peak amplitude and arrival time, the latter being proportional to the reinforcing steel depth in concrete. The use of SAFT required substantial modifications to the software package developed at CNDE for analyzing and distilling raw GPR data as measured previously.

The peak amplitude and arrival time data for each reinforcing steel target was determined. As was done in the earlier bridge study, the distilled GPR data were examined to locate anomalous

signals with unexpectedly low peak responses, and correlated with actual reinforcing steel damage as revealed by careful demolition of the barrier rail.

Laboratory Measurements and Analysis

When using GPR amplitudes to detect damage, the researchers were cognizant of the fact that reflected amplitude can be changed by many factors in addition to reinforcing steel thinning. These include the location and orientation of the reinforcing steel relative to the antenna, and the electromagnetic properties (principally wave speed and attenuation) of the local concrete volume in which the reinforcing steel is embedded. In the modeling portion of the work, the influence of these factors was investigated.

It was proposed to develop a laboratory simulation model capable of predicting the GPR response from a straight reinforcing steel segment having a thinned region (Figure 4). The dependence of the GPR reinforcing steel response was studied for various combinations of the degree of thinning, the position of the antenna relative to the thinned region, and the antenna tilt angle (θ) as shown in Figure 4.

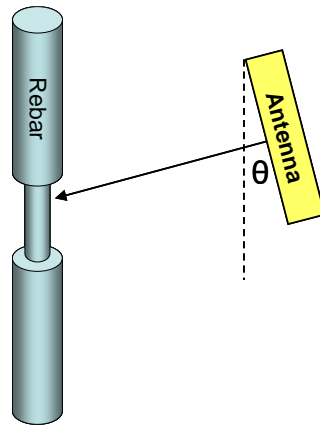


Figure 4. Assumed simplified geometry for thinned reinforcing steel

The model established an experimentally determined “tilt factor,” which summarizes the effect of antenna tilt on GPR response for reinforcing steel of various diameters. The extent and depth of the thinning was investigated by experimental measurements of how the GPR signal strength depends on the location and orientation of the reinforcing steel relative to the antenna. As illustrated in Figure 4, initial work did not focus on the concrete layer properties but considered the case where only air separates the antenna from the reinforcing steel. After validating the approach “in air”, the effects of concrete was approximately considered, taking into account both refraction at the air/concrete interface and the attenuation of electromagnetic (EM) waves by concrete.

In accounting for concrete properties, measurement schemes to determine EM wave speed and attenuation in concrete structures were developed. Both single antenna and double antenna approaches were explored, as illustrated in Figure 5.

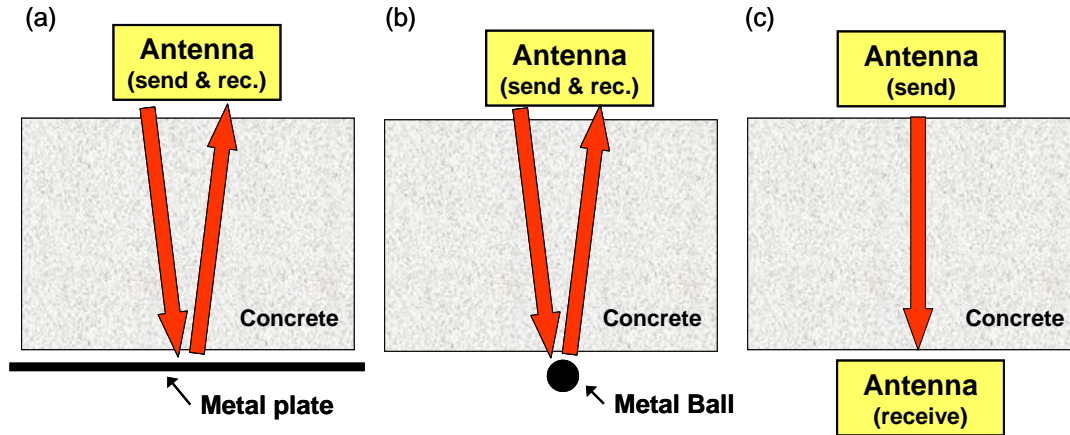


Figure 5. Measurement setups investigated for assessing concrete property variations within structures: (a) and (b) pulse/echo setups requiring only one GPR antenna and (c) pitch/catch setup requiring two antennas

Using a suitable concrete structure such as a retaining wall, measurements were made at multiple locations to determine the variability of local concrete properties within that structure. The simulation was then used to estimate how that variability affects GPR reinforcing steel amplitudes and, thus, how it affects the ability to reliably detect reinforcing steel thinning of various degrees.

MFL and Eddy Current (EC) Studies of Reinforcing Steel thinning Due to Corrosion

Based on the results of the feasibility study, further research and development was proposed as described below in order to improve the technical readiness of the electromagnetic techniques for inspecting reinforcing steel in bridge barrier rails.

Validation Study

Although consistent indications of possible reinforcing steel damage were obtained from the MFL and GPR field test data in Phase I, neither technique was validated through direct examination of the inspected reinforcing steel. In terms of MFL, Phase II included MFL field tests on highway bridges that are scheduled for replacement or repair. A commercial rebaroscope based on eddy current (EC) was used to help locate the depths of reinforcing steel under test and aid the analysis of MFL data. The bridge structures were demolished to validate the test results as described earlier.

Improvement of MFL Probe Design

The Phase I results revealed two specific areas of challenges for the MFL method, both of which were addressed in the research proposal. One is the development of a built-in reinforcing steel depth detection capability, and the second was to address the issue of interference by other reinforcing steel segments.

Currently, the MFL method is aided by an EC-based cover meter (e.g., rebaroscope) to determine the in-depth position of reinforcing steel in concrete structures. For the field test, it is desirable to be able to detect the reinforcing steel depth and reinforcing steel thinning using a single instrument. To this end, the study combined the magnetic reluctance (MR) measurement and MFL for inspecting reinforcing steel. The MR measurements were used to determine the reinforcing steel depth, while the MFL signals were used to detect reinforcing steel thinning as demonstrated in the Phase I study.

The probe design is shown in Figure 6.

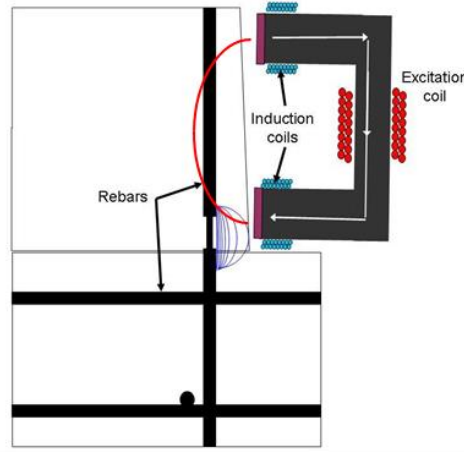


Figure 6. Probe design that combined magnetic reluctance and MFL measurements for inspecting reinforcing steel in concrete structures

The design is similar to the probe developed in Phase I, but included two additional induction coils located near the pole pieces. The coils were used to detect the amount of the magnetic fluxes flowing through the magnetic circuit. As illustrated in the figure, the circuit is comprised of a ferrite yoke, the reinforcing steel being tested, and a concrete layer. Note that the concrete layer can be treated as a non-magnetic layer in practice. The voltage output of the induction coil, $V_0^\mu(f)$, can be written as

$$V_0^\mu(f) = -\frac{d\Phi}{dt} = \frac{d}{dt} \left(\frac{N_{exc} I_{exc}}{R} \right) \quad (1)$$

where Φ is the magnetic flux through the detection coil, N_{exc} is number of turns in the excitation coil, and I_{exc} is the excitation current. The reluctance R is the analog of electrical resistance to the electric current, and represents the resistance of the medium against the magnetic flux passing through. Corresponding to the three magnetic circuit media, the total magnetic reluctance, R_T , of the magnetic circuit, has three components

$$R_T = R_Y + R_C + R_S = \frac{l_Y}{\mu_Y \mu_0 A_Y} + \frac{2l_C}{\mu_0 A_C} + \frac{l_S}{\mu_S \mu_0 A_S} \quad (2)$$

where R_Y , R_C , and R_S denote the magnetic reluctance of the ferrite yoke, the concrete layer, and the reinforcing steel, respectively. Similarly, A_Y , A_C , and A_S are flux cross sections in their respective regions. The outputs of the induction coils therefore provide a measure of the magnetic reluctance of the circuit, which strongly depends on the thickness, l_C , of the concrete layer covering the reinforcing steel. The effective path length, l_S , through the reinforcing steel will also have weak dependency on the standoff distance, which will be compensated for by calibration. In fact, the equivalent path length, l_S/μ_S , will be determined as such, thus not requiring predetermination of the relative permeability μ_S of the target reinforcing steel. The relative permeability μ_Y of the yoke material will be predetermined at the construction of the detector assembly.

As previously mentioned, the EC and MFL signals detected by the present sensor probes are susceptible to interference from other reinforcing steel near the cold joint. The research team addressed this issue by utilizing directional sensitivity. The sensor system that was developed, analogous to the one illustrated in Figure 6, has a directional sensing characteristic, meaning that it is selectively sensitive to the reinforcing steel parallel to the yoke orientation. Using a linear array of multi-axial magnetic field sensors for both the EC and MFL measurements reinforces this basic notion. Each of the sensors aimed to detect the EC field or leakage flux from defects in multiple directions. The goal was to map the magnetic field pattern and use it to separate the influence of nearby reinforcing steel from the defect signals. This separation occurs because a defect produces a distinctively different leakage field pattern from that of intact reinforcing steel. Under AC field excitation, both the amplitude and phase of the detected field signals can be used to correlate with the reinforcing steel bar size and distance from the sensor probe. This development alleviated the need for other techniques to survey the distribution of reinforcing steel in concrete structures under inspection.

Project Scope

In order to arrive at these future types of barrier rail inspections, more research was needed to validate the findings from the earlier feasibility study. Based upon the initial success of Phase I, a Phase II validation study was proposed. Phase II of the program focused on the validation of two of the methods used in the earlier work. Each of the methods (GPR and MFL) was refined to incorporate hardware development, along with a certain amount of modeling to aid in the quantification process. Each of the methods was implemented in an inspection/evaluation of a bridge barrier rail selected by the Iowa DOT. Upon completion of the inspection/evaluation, the bridge barrier rail was to be carefully taken apart to correlate the instrument assessment to that of actual corrosion present in the rail. Unfortunately, due to complications with the underlying structure of the bridge and miscommunication, the pieces of the reinforcing steel examined during both Phase I and Phase II were lost. Reinforcing steel in similar positions on the bridge was recovered, and correlation between the recovered north barrier rail and the examined south barrier will be discussed in the Test and Evaluation Results chapter.

SUMMARY OF PRIOR WORK

Problem Statement

The objectives of the Phase I research were as follows:

- Provide a comparison of three inspection methods—GPR, MFL, and radiography—for applicability to bridge barrier rail inspection
- Determine the quantitative capability of each method using controlled laboratory samples
- Provide a preliminary feasibility assessment that included a limited field test at a typical barrier rail construction bridge

Given the complexity of detection and quantification of buried structures such as reinforcing steel in concrete, there were several potential solutions for investigation, which included GPR, MFL, and radiographic inspection. Each method has advantages and disadvantages.

The Phase I feasibility study compared the sensitivity and cost effectiveness of each of the methods in a laboratory environment. In addition, limited field testing of GPR and MFL techniques was conducted.

Field testing of the radiographic technique was not planned for this Phase I work due to equipment portability constraints within the short duration of the project. (Recommendations included Phase II field prototype instrument development and a formal test.)

Results from Prior Work

Three technologies were evaluated for their ability to detect and quantify corrosion damage in reinforcing bars used in barrier rail geometries. A two-phase approach that included laboratory evaluation on typical sample geometries followed by a limited field feasibility study on the IA 210 Bridge over I-35 south of Ames, Iowa was completed. Application of radiography to this problem was limited to the laboratory evaluation as discussed below. Summaries for each method follow.

Radiography

X-ray radiography provides clear images of the condition of reinforcing steel in concrete. This has been demonstrated previously using film. To date, there has been a reluctance to use this technique due to the cost of equipment and the slow feedback for film radiography. In other laboratory studies, researchers were able to demonstrate that corroded reinforcing steel in concrete bridge barrier rails is easily located using digital radiography. This approach provides a feedback time of less than one minute per location. Furthermore, the image gives a direct visual measure of the extent of corrosion.

However, the equipment available in this study was not optimal for inspection of this type of object. In particular, the x-ray sources currently available in the research team laboratory are of relatively low power (320 kV). Although adjustment of the exposure parameters to obtain good images is feasible, a higher potential tube would be more efficient. The detector used was also quite bulky and inefficient for field application. Several digital x-ray imagers are available that would be more efficient for this application.

The simulation model, XRSIM, was useful in guiding the selection of the optimum setup parameters. The early experimental success meant that the researchers did not have to rely on XRSIM to extrapolate to higher energy sources. The comparisons made between experimental and simulated results indicated that the understanding of the scattering processes in such thick materials is incomplete. This insight will guide further fundamental work in developing simulations of the scattering process.

An x-ray backscatter configuration was also evaluated and showed some promise. However, the users were not able to consistently identify the location of the buried reinforcing steel. Earlier work indicated good results using a Cs-137 radioactive source (662 keV). This is much higher energy than the project's x-ray tube was capable of producing. However, a radioactive source requires much longer time for imaging, and raises security concerns. Linear accelerators (linac) can produce the required high energies without these concerns. It is recommended that backscatter studies be completed using a higher energy x-ray source.

It was not possible to evaluate either of these x-ray techniques on an actual bridge. This was due to the need to follow state regulations for x-ray system licensing and safety, which were beyond the scope of this short demonstration. There are companies that are already licensed to operate x-ray systems in an open outdoor environment in Iowa. As a follow up to these studies, it would be useful to contract with such a company to conduct some field tests.

Ground Penetrating Radar

The use of GPR was investigated to detect corrosion-induced reinforcing steel thinning in concrete bridge supports. The approach was based on observing the peak amplitude of the reflected GPR signal from embedded reinforcing steel. Other things being equal, localized thinning was expected to lower the GPR response, since thinned reinforcing steel presents a smaller reflecting target to the incoming electromagnetic pulse. In measurements on reinforcing steel-in-concrete laboratory specimens, amplitude change was able to reproducibly detect a 50% thinning condition but not a 25% thinning situation.

Field measurements were conducted at a local bridge where IA 210 passes over I-35. The approach was to look for a change in reinforcing steel response as the GPR antenna was "elevated" above the roadbed (i.e., moved away from the likely location of any corrosion-induced thinning). In several instances, antenna elevation resulted in a marked increase in reflected amplitude, consistent with expectations for reinforcing steel thinning at the roadbed. However, reflected amplitude can be changed by many factors in addition to reinforcing steel thinning (e.g., reinforcing steel location and orientation, concrete property variations, etc.).

Simulation models can be used to investigate the relative importance of such factors, and work was begun on developing such models for simulating the reinforcing steel inspection process. Use of radiography in the suspect locations would validate the GPR results. Destructive removal of concrete could also be used to verify condition.

Eddy Current and Magnetic Flux Leakage

A three-stage study was carried out using the EC and MFL techniques to evaluate the feasibility of detecting damage of reinforcing steels near the cold joint of bridge structures. A commercial EC-based reinforcing steel locator was acquired and a MFL sensor probe using GMR sensors was developed for the study. In stage 1, EC and MFL measurements were carried out on a set of bare, standalone #4 reinforcing steel bars with and without artificial defects. Both EC and MFL readily detected 25% and 50% material loss in the standalone reinforcing steel at the minimum required distance of 2.5 in. (63.5 mm). The EC and MFL signals were both found to decrease monotonically as the amount of material loss increased, indicating the potential of using these techniques to quantify material loss of standalone reinforcing steel.

EC and MFL measurements were conducted on mockup samples consisting of multiple #4 or #6 reinforcing steel bars, with or without artificial defects, which were embedded inside the concrete according to the design provided by Iowa DOT. Both EC and MFL signals were found to be affected by other reinforcing steels near the cold joint, but the signals detected away from the interfering reinforcing steel were dependent on the amount of local material loss of the vertical (anchoring) reinforcing steel. The results indicated the possibility of using the techniques to detect reinforcing steel damage in bridge structures, provided other methods are available to generate an independent survey of the distribution and orientation of reinforcing steels over the region of interest, so that the potential interference of other reinforcing steels on EC and MFL inspections could be minimized and quantified.

A field test was carried out on IA 210 over I-35. MFL line scans were performed on and off the bridge deck across a total of 18 reinforcing steel bars selected from 4 different sections of the bridge. Thirteen inspected reinforcing steel bars showed stronger off-deck MFL signals, suggesting possible damage in those reinforcing steel segments near the cold joint based on the results obtained from the mockup samples. By comparing the MFL and GPR scan results, it was found that MFL made the same predictions as GPR for 16 of 18 tested reinforcing steel bars.

Comparison of GPR and MFL Results

Since no destructive examination of the reinforcing steel bars was performed to validate the field tests, the GPR and MFL results were compared to determine whether the two techniques gave consistent indications of the suspected reinforcing steel conditions. Similar to the GPR tests, MFL scans were performed on the same sections by scanning the antenna on the bridge deck and scanning again after it was raised 1.5 in. off the deck in order to examine any change in signal that would indicate reinforcing steel damage.

When comparing the on-deck and off-deck GPR signals, most of the hyperbolae, each of which indicates the presence of a piece of reinforcing steel, showed the same on-deck and off-deck signal level, indicating that those reinforcing steels were possibly undamaged. The exceptions were those locations where hyperbolae showed a significant increase in the off-deck signal compared to the on-deck signal, suggesting possible reinforcing steel damage. In comparison, the MFL scan results were found to be consistent with the GPR data. Similar qualitative comparisons between the MFL and GPR field test data were made. The results are summarized in Table 1, which lists the predicted reinforcing steel conditions based on the MFL and GPR data.

Table 1. Comparison of MFL and GPR prediction of damage

	Crown				East end								West end			Section 4		
Rebar	C-1	C-2	C-3	C-4	E-1	E-2	E-3	E-4	E-5	E-6	E-7	E-8	W-1	W-2	W-3	CW-1	CW-2	CW-3
MFL	N	N	N	Y	N	Y	N	Y	Y	Y	Y	Y	Y	Y	Y	Y	Y	Y
GPR	N	N	N	Y	N	Y	N	N	Y	Y	Y	Y	N	NA*	Y	NA	NA	NA

Y=Positive indication of possible damage

N=No indication of possible damage

NA*=GPR data not available for comparison

It is evident that in most cases (16 out of 18 reinforcing steel bars) MFL presents the same predictions as GPR, except for reinforcing steel E-4 of the east end section and reinforcing steel W-1 of the west end section where MFL indicates possible damage while GPR does not.

TEST AND EVALUATION METHODOLOGIES

Discussion of Methodologies

Although there were three methods listed in the proposal, the Iowa DOT and CNDE agreed that the radiography method should be set aside. It was felt that the expense and potential public relations issues outweighed the benefits of the method, given that the plan called for exposure of the reinforcing steel for measurement of material loss. For this reason, only GPR and electromagnetic methods are discussed.

Evaluation of GPR Methods

GPR is routinely used to locate and map steel reinforcing bars (reinforcing steel) in concrete structures. Detecting damage to embedded reinforcing steel is a much more difficult challenge. The equipment used in the project measurements is shown in Figure 7.

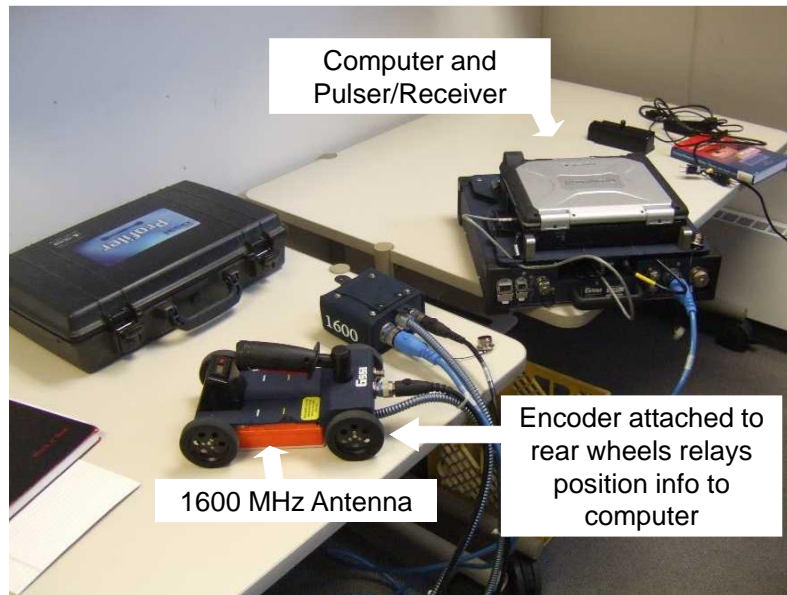


Figure 7. Portable GSSI ground penetrating radar equipment employing a single 1600 MHz antenna

The commercially available, portable, battery operated, GPR unit was manufactured by Geophysical Survey Systems, Inc. (GSSI).

The pulser portion of the pulser/receiver sends a voltage pulse along the coaxial cable leading to the antenna. This produces a short-duration EM pulse radiated by the antenna. Some of this radiated EM energy strikes an embedded reinforcing steel bar and is reflected back toward the antenna. When it is received, an output voltage signal in the coaxial cable results, which is then amplified by the receiver electronics and displayed on the computer monitor.

As indicated in Figure 8, the GPR inspection process is analogous to that used in pulse/echo ultrasonic inspection, and tools developed on the ultrasonic side for analyzing data and modeling inspections can be readily adapted to GPR.

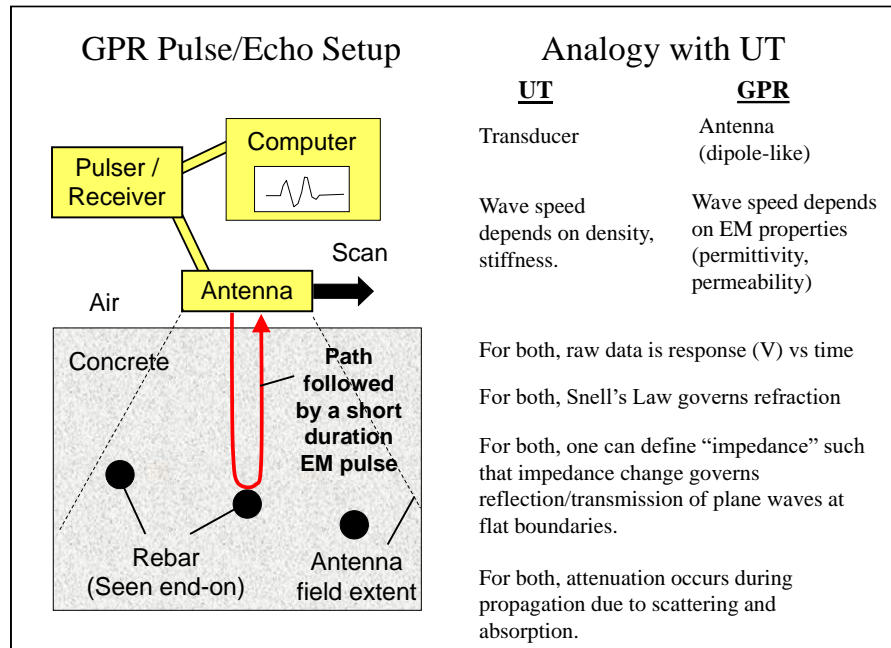


Figure 8. GPR pulse/echo inspection of reinforcing steel, and analogy with ultrasonic inspection

For a one-dimensional scan of the antenna, a standard GPR display is referred to as a B-scan, with an example shown in Figure 9b. The horizontal axis indicates the transducer position, while the vertical axis displays either signal arrival time or inferred penetration depth. The gray-scale image then depicts echo strength, with white depicting a strong positive voltage value, and black a strong negative voltage.

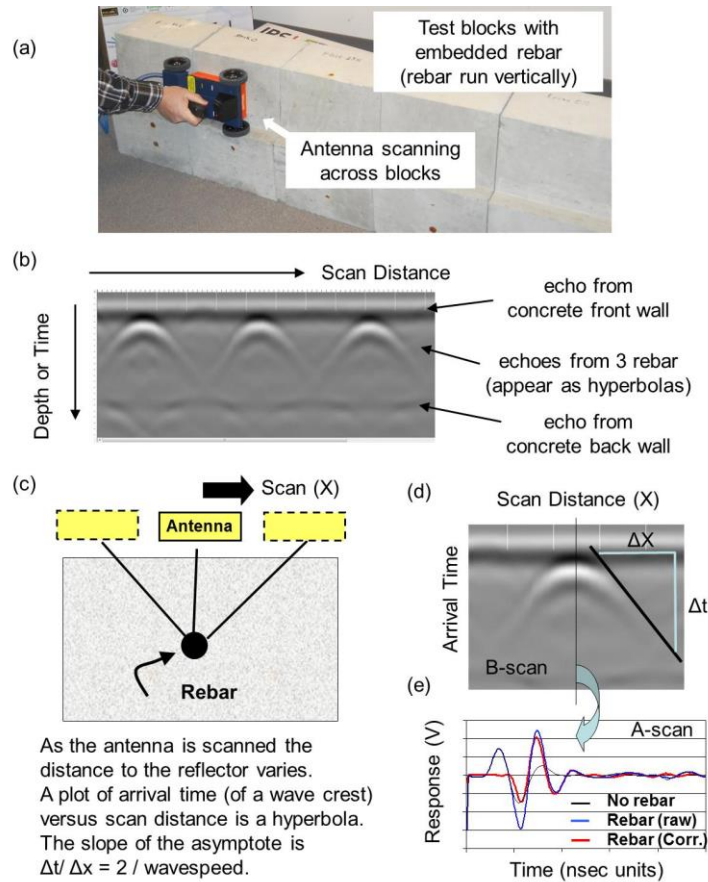


Figure 9. (a) Scan of GPR antenna across three abutting test blocks each containing one embedded reinforcing steel bar, (b) resulting B-scan image, (c) and (d) why reinforcing steel B-scan responses have a characteristic hyperbola shape, and (e) GPR A-scan plot of output voltage versus time for antenna position indicated by vertical black line in panel (d)

The signal-voltage-versus-arrival-time plot observed at any fixed antenna position is called an A-scan or “wiggly plot” and an example is shown in Figure 9e. For the standard 1600-MHz antenna that was used, the EM radiation is in the microwave band. The wave speed and wavelength in concrete depend on the dielectric constant of the concrete, which varies somewhat for different grades of material. Typically, the wavelength in concrete is on the order of a few inches, and the reinforcing steel diameter is thus smaller than either the EM wavelength or the broadcast envelope (radiation pattern size) of the antenna.

When the antenna is scanned across a concrete fixture containing a reinforcing steel section (Figure 9a), the reinforcing steel is "sensed" at many different antenna positions. The arrival time of the reinforcing steel echo depends on the distance between antenna and the reinforcing steel, and is smallest when the antenna is directly above the reinforcing steel. Because of the dependence of echo arrival time on antenna position, regions of high reflected amplitude in B-scans have a hyperbola-like shape as illustrated in Figure 9d. The slope of the hyperbola's asymptote depends on the EM wave speed in concrete. A measurement of that slope can be used

to infer the wave speed and, hence, the dielectric constant of concrete on which the wave speed depends. This will be explicitly demonstrated later.

Figure 9a shows the GPR antenna being run across three abutting test blocks, each containing one embedded reinforcing bar, to obtain a scan, and Figure 9b shows the resulting B-scan image. Figures 9c and 9d show why reinforcing steel B-scan responses have a characteristic hyperbola shape. Figure 9e shows the GPR A-scan plot of output voltage versus time for the antenna position, indicated by the vertical black line in Figure 9d.

In some practical cases of interest, the echo from the reinforcing steel partially overlaps the earlier-arriving echo from the air/concrete interface immediately below the antenna. Analysis tools can be used to “subtract” the air/concrete echo, resulting in a “reinforcing steel only” A-scan, as demonstrated in Figure 9e.

Evaluation of Electromagnetic Methods

A study was carried out to evaluate the potential of MFL for detecting corrosion damage to anchoring reinforcement bars near the cold joint between the road deck and barrier rails of bridges. In the first stage of the study, MFL measurements were carried out on standalone #4 reinforcing steels with and without artificial defects of 25% and 50% material loss, using a MFL system that was developed by using GMR sensors to detect leakage fluxes from defects in reinforcing bars. The MFL technique can detect the reinforcing bar at a distance of 2.5 in. The amplitude of the MFL signal varies monotonically with the amount of material loss, indicating the potential of using the techniques to quantify material loss of standalone reinforcing bars.

In the second stage, MFL measurements were conducted on mockup samples described previously in the Discussion of Methodologies section. MFL signals were found to be affected by a horizontal reinforcing steel bar underneath the cold joint. Nevertheless, the signals detected away from the interfering reinforcing bar are dependent on the amount of material loss of the vertical anchoring reinforcing steel near the cold joint, suggesting the possibility of using the technique to detect reinforcing bar damage in bridge structures.

In the third stage of the feasibility study, a limited field test was carried out on IA 210 over I-35 in Iowa, with the aim of evaluating the technique in field conditions where the actual arrangement of reinforcing bars could be more complicated. Several MFL line scans were performed at one location of reinforcing steel. Unfortunately, shortly after testing began, two issues arose that called for the cancellation of the tests. The equipment, which was not designed to work in the field, stopped working, and the time limit to have the lane closed for inspection expired, ending the testing session.

TEST AND EVALUATION OF RESULTS

Ground Penetrating Radar Laboratory Results

This section reports on GPR studies continued from work begun in 2012 in the first phase of this project. The goal was to develop a GPR-based bridge inspection technique aimed at identifying the unsafe condition where corrosion had thinned the reinforcing steel that attaches the side barrier rail to the bridge deck to the extent that the rail could no longer withstand typical impacts. By quantifying corrosion, a suitable nondestructive test will enable reinforcement of only those barrier rails that are no longer safe and, thus, increase bridge safety while reducing overall repair costs. The work suggested that the amplitudes of GPR signals could be used to differentiate intact reinforcing steel from those sections having substantial corrosive metal loss. However, many factors can potentially contribute to the strength of the echo observed from a given reinforcing steel segment, including the length of the reinforcing steel, its position and orientation relative to the GPR antenna, and the location and size of the metal loss region.

Laboratory Measurements of GPR Signal Attenuation in Concrete

Many setups can be used to measure the EM attenuation of a test specimen, and some of these are pictured in Figure 10a.

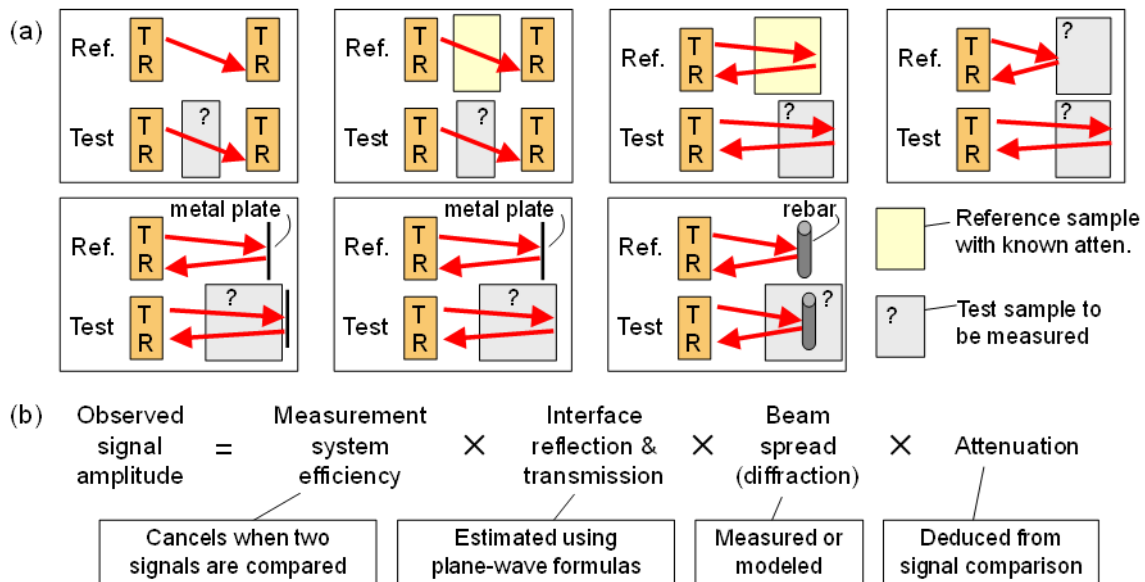


Figure 10. (a) Some of the many possible setups for normal-incidence attenuation measurements and (b) general form of the model expression used in attenuation deduction

Each GPR antenna (or more accurately “antenna housing”) actually contains two separate bow-tie antennas: one for signal transmission (T) and one for reception (R). Researchers use the terms “pulse/echo” (P/E) and “pitch/catch” (P/C) to refer to inspections, which use one or two antenna housings, respectively. Because of the dual-bow-tie nature of each antenna, P/E measurements

are complicated by the appearance of “direct-coupled” signals in which EM energy travels directly from the transmitter to the receiver.

In general, comparison is done for two or more signals whose difference depends in part on the attenuation of the test specimen. These signals may be obtained from the test specimen alone (e.g., reflections from the front and back surfaces), or from different specimens (e.g., the test specimen and a reference specimen). When comparing the two signals, corrections are made for interface losses, beam spread, and differences in equipment amplification levels. Any remaining difference between the two signals is then assumed to be due to attenuation, allowing the unknown attenuation of the test specimen to be deduced. Typically, attenuation is quantified by using units of decibels of signal amplitude loss per inch of travel (dB/in). In deducing attenuation, researchers made use of model-based expressions, which are the GPR analogues of those used in ultrasonic measurement. As illustrated in Figure 10b, the observed response for either the “reference” or “test” measurement is written as a product of four factors, which, respectively, account for the measurement system efficiency, losses at interfaces, and losses due to beam spread and attenuation. Strictly speaking, the approach of writing the observed response as a product of four factors applies in the frequency domain where amplitude refers to the spectral magnitude of the response at some specific frequency. But the approach can also be used, albeit less accurately, in the time domain where amplitude is interpreted as, say, the maximum peak response of the early-arriving portion of the GPR signal.

Beam-Spread Corrections

For the 1.6 GHz antenna, the physical dimensions of the bow-tie elements (a few inches) are smaller than a wavelength in air (7.4 in. at the nominal center frequency). Consequently, the radiation pattern for the antenna is not much different from that of a point source, and spreads rapidly with distance. This spreading, or diffraction, can have a strong influence on GPR signals and must be accounted for in attenuation measurements. One of the pitch/catch measurement setups considered is that shown in the upper left portion of Figure 10a.

The effect of diffraction on the reference signal can be determined using the approach illustrated in Figure 11.

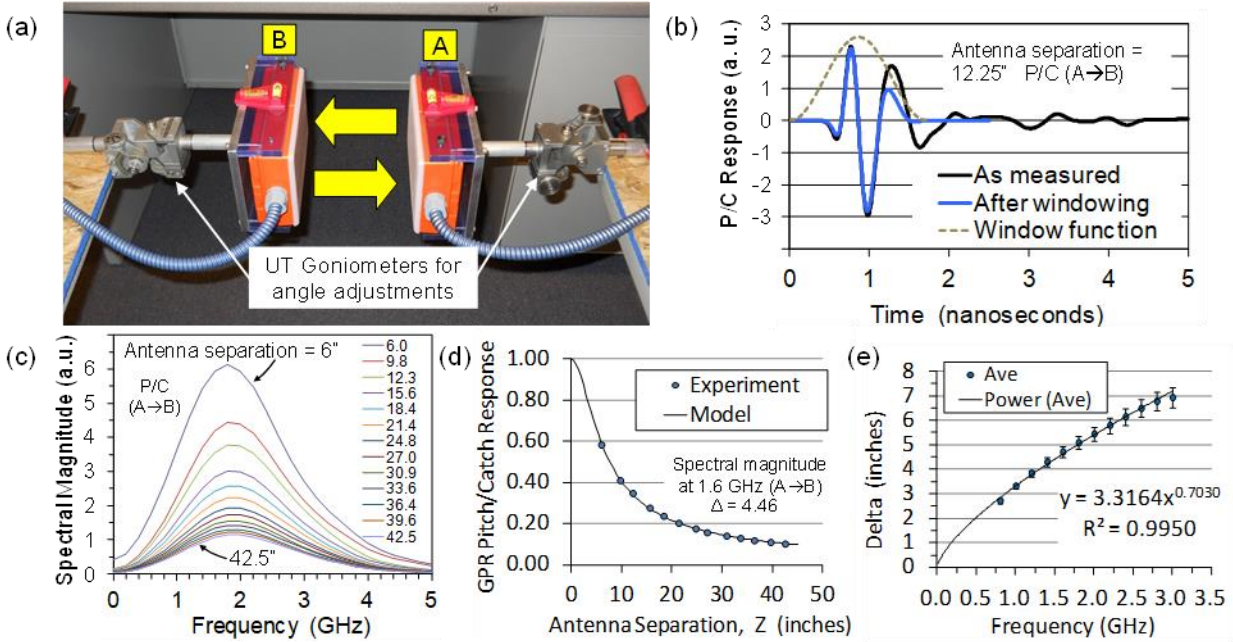


Figure 11. (a) Pitch/catch setup for measuring beam-spread effects in air, (b) typical raw GPR signal before and after windowing, (c) spectral magnitudes of measured signals for different antenna separation distances ranging from 6 to 42.5 in., (d) measured and fitted spectral magnitudes at 1.6 GHz, and (e) dependence of the parameter Δ on frequency

The two antennas are positioned to face one another with their centers aligned. The pitch/catch GPR signal is then measured for a series of separation distances with one antenna (A or B) acting as the transmitter and the other as the receiver. Both measurements (A→B and B→A) can be performed together using separate channels of the GPR instrument. A typical measured time-domain signal (A-scan, or “point scan”) is shown in Figure 11b.

For attenuation measurements, the researchers preferred to work with the early-arriving portion of the GPR signal since this tends to be less affected by reverberations within layers and other later arriving spurious signals. When computing spectral components of signals, a windowing function was applied to the early arriving portion. The researchers followed the method of Lai et al. (2010), where a Hanning window (cosine bell window) is used. The duration of the windowing function is fixed at approximately eight times the separation between the dominant positive and negative peaks of the early-arriving portion of the signal, and the window center is placed at the intervening zero-crossing time. The effect of windowing is demonstrated in Figure 11b for one case. Figure 11c shows computed spectra of windowed signals obtained for a range of antenna-to-antenna separation distances. The intent was to increase the separation distance by 3 in. between measurement trials, but the actual spacing varied somewhat. The antennas were each attached to rolling tables. It proved easiest to shift one table by an approximate amount, check antenna alignment, and then accurately measure the resulting separation. As shown in Figure 11c, the measured response at a given frequency falls steadily with increasing antenna separation. However, the rate of fall is smaller at higher frequencies where the radiation pattern of each antenna is more directed and less like that of a point source. For a given frequency, the spectral magnitude can be plotted as a function of separation distance as shown in Figure 11d for

the 1.6 GHz component. Because attenuation in air is very small here, the response drop-off seen in Figure 11d can be wholly ascribed to beam spread.

In order to apply beam-spread corrections when the attenuation of concrete specimens is determined, it is convenient to replace measured data with a simple fitted function. The researchers chose a functional form taken from an ultrasonic testing (UT) analogy, that of two identical Gaussian-profile transducers separated by a distance Z in a non-attenuating fluid. For that case, the diffraction correction, normalized to 1 at zero separation, has the form:

$$D(z) = \Delta / \sqrt{z^2 + \Delta^2} \quad (\text{assuming paraxial approximations}) \quad (3)$$

Here the parameter Δ , with units of length, serves as a frequency-dependent fitting parameter. In the UT analogy, Δ increases with both frequency and transducer diameter. Although this form is not expected to apply exactly in this GPR case, it does have the proper $1/Z$ asymptotic fall-off rate at large Z , as well as the ability to incorporate different fall-off rates at different frequencies. In practice, it was found to do an adequate job of summarizing the measured data, as the example in Figure 11d indicated. Within the bandwidth of these measurements, the best-fit value of delta was found to increase steadily with the frequency in the manner shown in Figure 11e. Minor differences were seen in the measured signals depending on which antenna (and its associated powering circuitry) was used as the transmitter and which as the receiver. These A→B and B→A signal differences led to minor differences in fitted Δ values as indicated in Figure 11e where the plotted point is the average of the two delta values and the error bar is their difference. Figure 11e also indicates a power-law fit to the Δ -versus-frequency data, which was later used to estimate Δ values (and hence beam-spread factors via Equation 3) for subsequent attenuation measurements.

Of course, Equation 3 and the associated Δ power law only apply directly to GPR beam spread in air. To compute beam-spread factors for layered structures (such as the antenna/air/concrete/air/antenna), researchers used a paraxial approximation based on Snell's Law of Refraction as illustrated in Figure 12d.

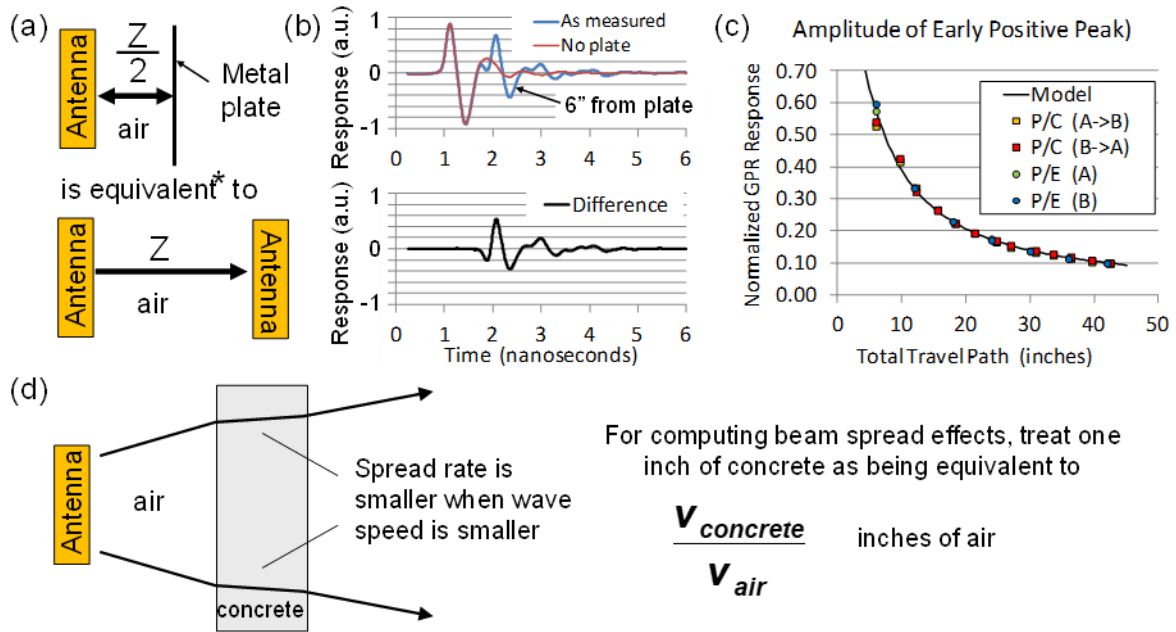


Figure 12. (a) Equivalence (under paraxial approximations) between pulse/echo and pitch/catch beam-spread measurement setups for two identical antennas, (b) pulse/echo signal reflected from a metal plate in air before and after subtraction of the direct-coupled signal, (c) comparison of (broadband) beam-spread effects for pulse/echo and pitch/catch measurements, and (d) handling of beam-spread corrections in concrete

The team assumed that beam spread rates in different media are proportional to the wave speeds in those media. For example, if the EM wave speed in concrete (v_c) is three times smaller than that in air (v_a), the lateral spread rate during propagation is then three times smaller in concrete than in air. Thus, the lateral spread that occurs while traversing 6 in. of concrete would be the same as that seen while traversing 2 in. of air, other factors being equal. Under this approximation, it was assumed that the effect of traversing Z_a in. of air and Z_c in. of concrete (in any order) is equivalent to traversing $Z_a + Z_c(v_c/v_a)$ in. of air alone. This stratagem allows the researchers to compute diffraction correction factors for multi-layer structures from the “air only” formula of Equation 3.

Beam-spread factors can also be measured using a pulse/echo setup, as illustrated in Figure 12a. One reflects the broadcast field from a large planar reflector oriented at normal incidence. In this case, a large aluminum plate was placed on the floor, and the antenna was aimed downward at it. One complication in pulse/echo measurements is the presence of the direct-coupled signal, which will partially overlap some or all of the signals of interest. This problem can be circumvented by separately measuring the direct-coupled signal and then, subtracting it from other measured signals, as illustrated in Figure 12b. To acquire the direct-coupled signal, the researchers rotated the antenna 180 degrees so that it pointed upwards toward the ceiling 6 ft away, guaranteeing there would be no large reflected signals within the first 12 nanoseconds following the direct-coupled signal. One comparison of beam-spread effects measured by different methods is shown in Figure 12c. There the early positive peak amplitude of each measured signal was plotted as a function of the total travel path through air, Z . There are four curves shown corresponding to P/E

measurements using antennas A and B in turn, and P/C measurements for A→B and B→A. Each curve has been normalized to have a common value at Z = 18 in. Modest differences were seen in the behaviors of the two antenna housings (and their associated circuitry) with regard to the appearances and amplitudes of measured signals. But the effects of these differences on beam-spread factors was judged to be relatively small. The same functional form used to fit single-frequency data (Equation 3) can be applied to the broadband data in Figure 12c as well. Such a fit to the combined data in Figure 12c resulted in a Δ value of 4.21 in. or close to that seen in Figure 11d for a fixed frequency of 1.6 GHz (Eisenmann et al. 2014, Eisenmann et al. 2015).

Attenuation Measurements for Concrete Patio Blocks

Having measured the beam spread factors in air for these antennas, it was now relatively straightforward to determine attenuation values for flat concrete specimens if some reasonable approximations were adopted. This was demonstrated by using a set of four nominally 16 x 16 x 2 in. concrete patio blocks obtained from a local home improvement store (Figure 13). Because the attenuation in these blocks was quite low (< 0.5 dB/inch), beam-spread effects must be treated if accurate results were desired.

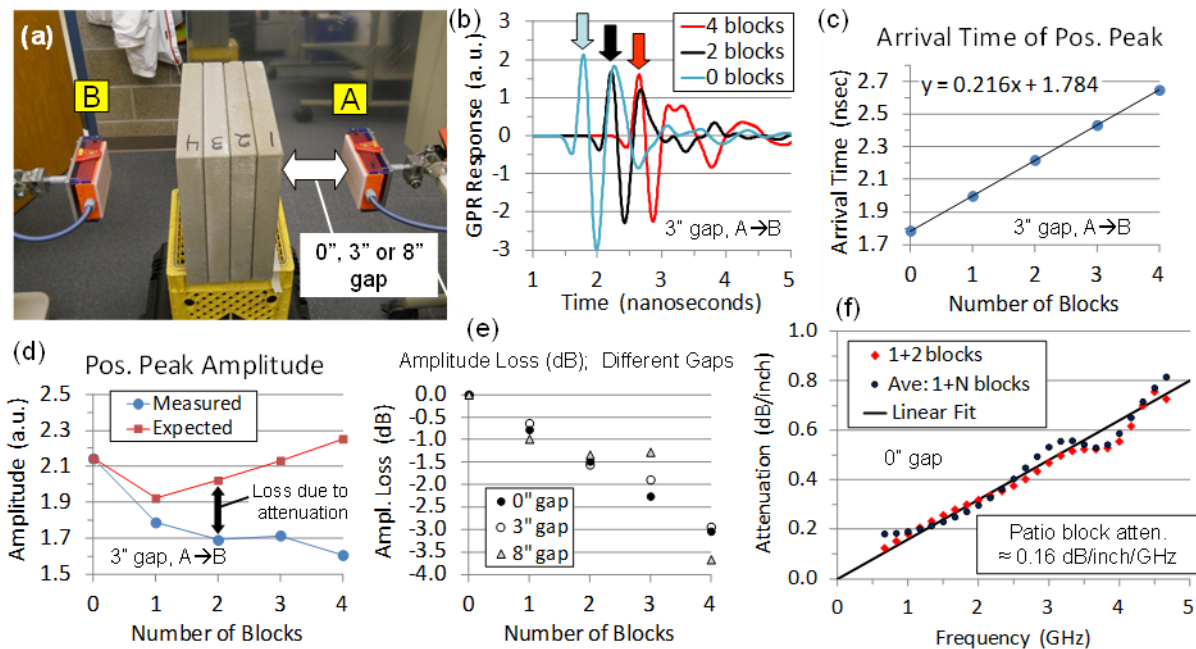


Figure 13. Attenuation measurements on concrete patio blocks: (a) setup phase, (b) raw GPR signals for one case (3-in. gap), (c) arrival time graph used to deduce EM wave speed in concrete for one case (3-in. gap), (d) amplitude fall rate for one case (3-in. gap), (e) amplitude loss in decibels relative to 0-block signal, and (f) attenuation versus frequency as deduced from spectral magnitudes of windowed signals

The pitch/catch measurement setup used is shown in Figure 13a. The two antennas were positioned 24 in. apart, and four abutting patio blocks were placed between them. Three trials were conducted in which the air gaps between block #1 and antenna A were 0, 3, and 8 in.,

respectively. For each trial, GPR data was gathered as the blocks were removed one at a time, beginning with the block furthest from antenna A (block #4 in Figure 13a). For the trial using the 3-in. gap, Figure 13b shows three of the five measured GPR signals, and indicates the early-arriving peak positive amplitude points used for quantifying signal arrival times and amplitudes. As the blocks were removed, the through-transmitted signal arrived earlier and its strength increased. The arrival times and amplitudes were plotted in Figures 13b and 13c, respectively. Because the speed of EM waves in concrete (v_c) was slower than that in air (v_a), an increase of Δz in the thickness of concrete traversed (and corresponding decrease of Δz in the thickness of air traversed) caused a delay in signal arrival time of $\Delta t = \Delta z/v_c - \Delta z/v_a$. Thus, from the slope of the best-fit straight line in Figure 13c and the known block thickness (2.09 in.), the wave speed in concrete was estimated.

An average over all trials yielded $\langle v_c \rangle = 5.301$ in/ns for the patio block wave speed, and a corresponding index of refraction of $n_c = v_a/v_c = 2.226$. Having determined the refractive index of concrete patio blocks, the standard plane wave formulas were used to estimate reflection and transmission coefficients at air/concrete interfaces (Eisenmann et al. 2014). In doing this, it was assumed that a group of N abutting blocks behaves as a single block of thickness $N\Delta z$. This led to a primary interest in the product of transmission coefficients $T_{a \rightarrow c} T_{c \rightarrow a} = 4 n_c / (1 + n_c)^2$, which governs the overall effect of transmission losses when one or more patio blocks are present. In Figure 13d, two sets of amplitudes are shown: those measured (circles) and those expected if the attenuation of concrete were zero (squares). The latter were computed by beginning with the measured amplitude for the no-block case, and making corrections for the interface loss factor ($T_{a \rightarrow c} T_{c \rightarrow a} = 0.855$) and for beam spread (using Equation 3 and the broadband average of $\Delta = 4.21$). The vertical separation between the points in Figure 13d then quantified the inferred signal reduction due to attenuation alone, under the researchers' approximations. The correction associated with beam spread alone (about a 6% decrease in signal amplitude as each block is removed) was significant compared to the measured amplitude changes. Plotting the attenuation-induced signal amplitude loss in dB (relative to a no-block reference) as in Figure 13e then led to a broadband estimate of attenuation loss of about 0.75 dB/block or 0.35 dB/in.

The last panel in Figure 13 summarizes the estimated frequency-dependent attenuation of patio block concrete. This was determined through a frequency-by-frequency comparison of spectral amplitudes of the signals for the gap = 0 in. case. The one-block signal was used as a reference so as to not require knowledge of the effective transmission coefficient at the interface between the abutting antenna housing and the first block, since this coefficient is then common for measurements with 1, 2, 3, or 4 blocks present. As in Figure 11b, an equivalent Hanning window was used to isolate the early-arriving portion of each signal prior to the zero padding and fast Fourier transform (FFT) computations used to determine spectral magnitudes. The red points in Figure 13f resulted from a comparison using only the one-block and two-block signals. The black points signify an average over three gap = 0 in. analyses using 1 and 2 blocks, 1 and 3 blocks, and 1 and 4 blocks, respectively. The deduced attenuation of the patio blocks rose approximately linearly with frequency and had a magnitude of about 0.16 dB/in./GHz.

In examining Figure 13e, there is less scatter about the trend line for the gap = 0 in. case compared to the gap = 3 in. and gap = 8 in. cases. Hence the use of gap = 0 in. measurements for determining attenuation-versus-frequency. The source of the scatter in Figure 13e was traced to

GPR signals arising from other travel paths that interfered (constructively or destructively) with the primary signal of interest here (direct transmission from transmitter to receiver through any blocks present). This is illustrated in Figure 14.

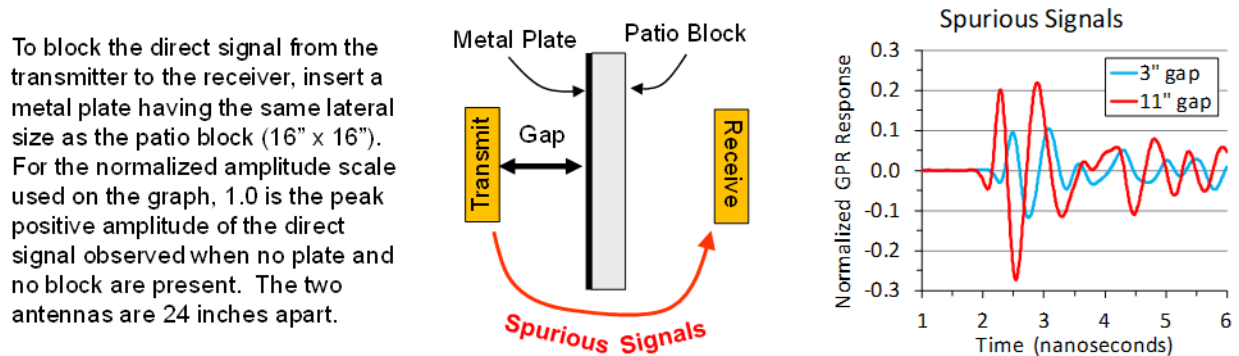


Figure 14. Simple measurement setup used to quantify strengths of spurious GPR signals associated with travel paths that bypass blocks under study

For various gap choices, a 16 x 16 in. metal plate was placed on the transmitter side of block #1 to preclude EM waves from traveling directly through the block. However, EM waves could diffract around the block (or reflect from fixtures and other objects in the laboratory) resulting in small received signals. Examples of these spurious signals are shown in Figure 14. Although such signals travel longer paths (in air) than signals of interest, they can arrive at the same time as the latter, which are naturally delayed by their passage through concrete. Such spurious signals lead to scatter in plots such as Figure 13e, and to waviness in attenuation-versus-frequency plots (such as Figure 13f). The effects of spurious signals tend to be greater for measurements using thick concrete specimens, since the primarily through-the-concrete signals are weaker and arrive later where spurious signals are more likely to be seen.

Attenuation Measurements on CAST Concrete Blocks

To further assess the utility of applying UT-based attenuation measurement methods to GPR, a second study was initiated using poured concrete blocks. Unlike the patio blocks, the new blocks contained sizeable aggregate particles in addition to sand and cement. By weight, the new blocks were fabricated from a concrete slurry containing 35% limestone aggregate (0.5-in. size), 33% river sand, 23% Holcim Type III cement, and 9% water. This mixture was cast into four blocks having nominal dimensions of 16 x 16 in. x Z, with Z equal to 2 in., 4 in., 6 in., and 8 in., respectively. The blocks were cured for two weeks prior to the measurements described here. Thus far, only the 2-in. and 4-in. blocks (having average thicknesses of 2.14 in. and 4.21 in., respectively) have been examined using GPR.

The attenuation measurement setups used to examine the cast blocks are indicated in Figure 15a.

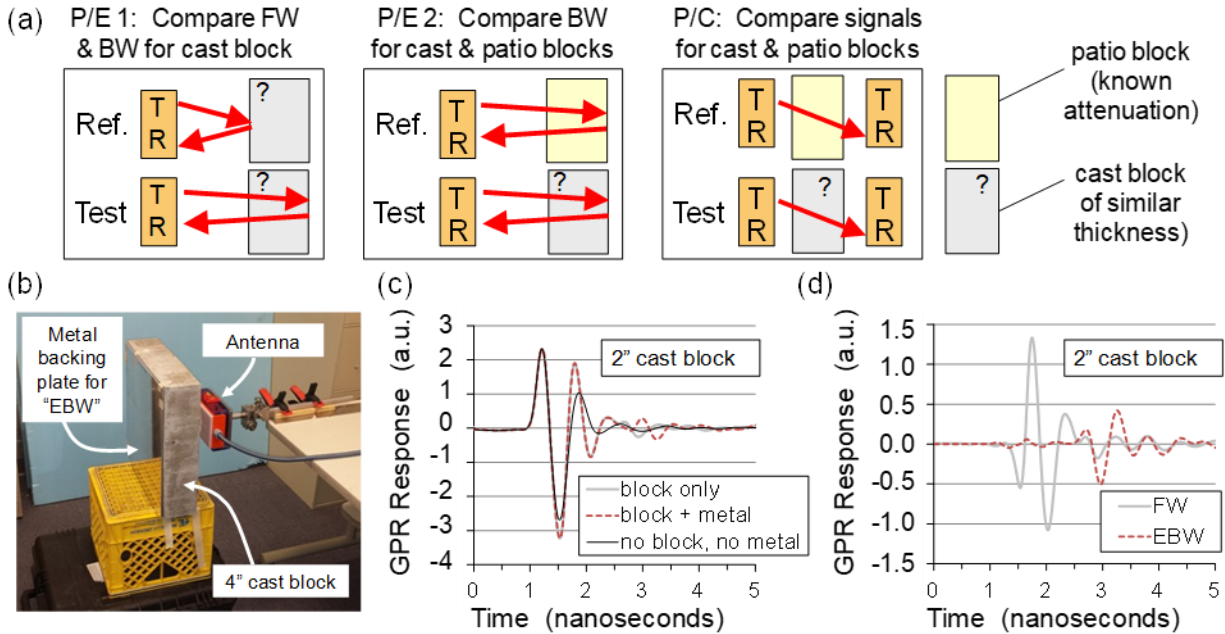


Figure 15. (a) Setups for attenuation measurements on cast concrete blocks (24-in. antenna separation for P/C), (b) cast block with metal plate in place for enhanced back-wall (EBW) echo acquisition, (c) raw GPR signals for setup P/E-1 using 2-in. cast block, and (d) resulting front wall (FW) and EBW echoes (prior to windowing) deduced by signal subtraction

All are analogues of setups commonly used for water immersion UT attenuation measurement. In the first P/E setup (P/E-1), the front wall (FW) and back wall (BW) echoes from the cast test block were compared. In the second P/E setup (P/E-2), the BW echo from the cast block was compared to that of a reference block, in this case a patio block (or pair of abutting patio blocks) of the same nominal thickness. In the third setup (P/C), early arriving through-transmitted signals for cast and reference blocks of similar thickness were compared. In each case, the standard Hanning window was applied to the signal in question, the FFT of the windowed signal was computed, and the resulting spectral amplitudes were corrected for the effects of beam spread, losses at interfaces, and the attenuation of the reference patio block (if used). Thus, from the two signals being compared, the researchers deduced the attenuation of the cast block at frequencies within the useable bandwidth of the GPR equipment. This also required an estimate of EM wave speed in the cast concrete. This speed was estimated from the arrival times seen in P/C measurements with and without the cast block present, leading to an average wave speed of 3.650 in./ns and an associated refractive index of $n_c = 3.234$.

For the P/E GPR measurements, one modification generally not used in UT measurements was adopted. Rather than using BW echoes as directly measured for the setups of Figure 15a, enhanced back-wall (EBW) echoes were used. These were obtained by placing a 16 x 16 in. metal plate in contact with the back wall of the test or reference block, as shown in Figure 15b. A GPR signal was first acquired without the plate, then one with the plate, and then the latter was subtracted from the former. This subtraction acted to (1) remove signals not arising from BW reflections and (2) enhance the strength of the BW signal. The latter occurred because the

“without metal” and “with metal” signals are 180 degrees out of phase. The raw BW signals with and without metal present are proportional to their respective reflection coefficients, $R_{c \rightarrow a} = (n_c - 1) \div (n_c + 1) = 0.528$, and $R_{c \rightarrow m} = -1$, respectively. The EBW echo is consequently proportional to $R_{c \rightarrow a} - R_{c \rightarrow m} = 1.528$. The signal subtractions used to obtain EBW echoes are illustrated in Figure 15c for one case. The subtraction leading to EBW signals automatically removed the direct-coupled signal. To obtain FW signals for use in P/E-1, the direct-coupled signal must also be subtracted. Again, this was done by subtracting the signal acquired with no blocks present and the antenna pointing away from any laboratory structures. For P/E measurements, a (nominal) 3 in.-separation was placed between the antenna and the concrete block to allow a relatively clean observation of the FW echo.

Figure 16 summarizes the deduced attenuation values for the 2- and 4-in. thick cast blocks. Three curves are shown for each block corresponding to the three methods indicated in Figure 15a.

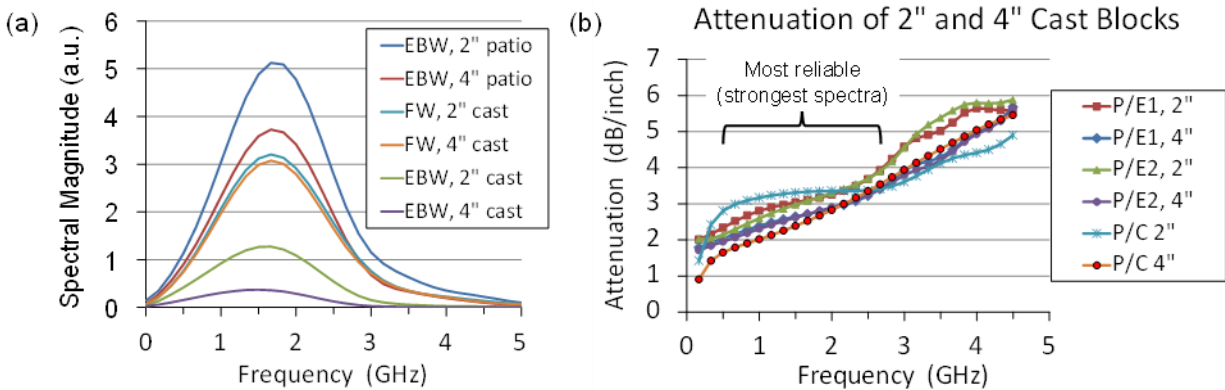


Figure 16. (a) Spectral amplitudes for some of the signals involved in determining attenuation of 2-in. and 4-in. thick cast blocks and (b) deduced attenuation-vs-frequency curves for cast blocks using various methods

The attenuation curves are expected to be most reliable near the centers of the bandwidths of the signals used in the analysis (Figure 16a), from about 0.5 to 2.5 GHz, but results have been shown for a wider range in Figure 16b. In the ideal case, assuming both specimens to be equally cured and subject to rigorously correct measurement procedures and analyses, the six curves in Figure 16b would exactly overlap. This is only approximately the case for the methods and approximations used in this study. Different methods give somewhat different results, although the general trends are very similar. Some of the departures from the norm can be traced to specific causes. For example, for the pitch/catch measurement on the 2-in. block [P/C (2 in.)], the pronounced wiggles were apparently due to interference between the signal transmitted through the block and one diffracted around the block. On average, near the nominal center frequency of 1.6 GHz, the attenuation of the cast blocks was found to be about 10 times that of the patio blocks. One peculiarity in Figure 16b concerned the low-frequency behavior of the curves. Researchers expected the attenuation to trend to zero at zero frequency, but this behavior was not evident. It may be that the attenuation of the cast material dropped rapidly to zero below 0.5 GHz. More likely, there was some systematic effect present, resulting from the approximations and analyses used that caused deduced attenuation curves to shift upward. Systematic errors may

spring from the use of Hanning windows to isolate signal attributes. This sort of windowing is not typically needed in ultrasonic attenuation measurements where FW and BW signals are generally well-resolved, and spurious signals are not present.

Laboratory Measurements in Air: Effect of Reinforcing Steel Position, Orientation, and Metal Loss on GPR Signals

The peak amplitude of a reinforcing steel response can be affected by factors other than metal loss, such as the depth of the reinforcing steel in concrete (and associated signal losses due to beam spread and attenuation) or the orientation of the reinforcing steel relative to the antenna. To field a practical amplitude-based system for detecting corrosion-thinned reinforcing steel, it is critical to be able to assess and account for such factors. This section contains a discussion of the initial experiments aimed at quantifying such effects. For convenience, the measurements were performed using reinforcing steel in air rather than reinforcing steel embedded in concrete. This gave the researchers the freedom to easily vary the inspection geometry. The next section will discuss the researchers' efforts to move a step closer to investigating reinforcing steel embedded in concrete by surrounding the reinforcing steel with a powdered material having similar GPR properties to concrete.

The antenna-based coordinate system is illustrated in Figure 17a.

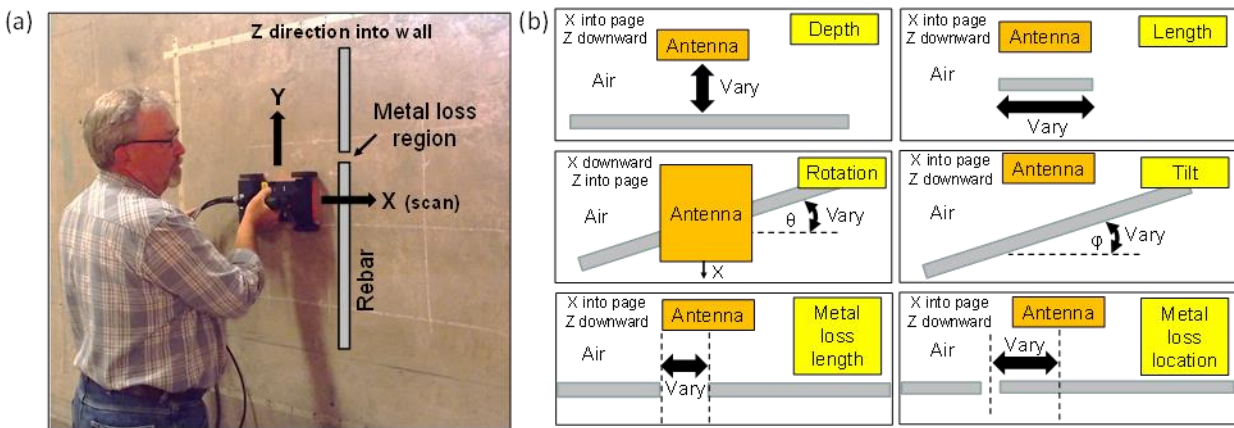


Figure 17. (a) Coordinate system centered on the GPR antenna and (b) setups used for measurements of reinforcing steel in air

The positive X-axis is the traditional scanning direction of the antenna, which happens to be parallel to the longest dimension of the antenna housing. GPR pulses are launched in the Z direction, which is parallel to the thinnest dimension of the housing. The gray rectangle in Figure 17a depicts an embedded reinforcing steel bar at some depth in the wall, which is oriented parallel to the Y-axis. In this scanning orientation, the electric field vector of the outgoing EM pulse is polarized approximately parallel with the reinforcing steel length, leading to a maximal backscattered signal. This is a consequence of the orientations of the bow-tie antennas within the housing. The reinforcing steel depicted in Figure 17a is shown with a gap representing missing metal, perhaps as a consequence of corrosive loss. For the air measurements, a gap was

introduced to simulate loss of metal. This was done by simply abutting two reinforcing steel lengths end-to-end and then pulling them apart at a fixed distance.

Figure 17b illustrates the six measurement setups for which the GPR reinforcing steel response was studied while a key geometric parameter was varied. The parameters were as follows:

1. The “depth” or distance Z from the bottom of the antenna housing to the top of the reinforcing steel (using a long reinforcing steel bar centered beneath the antenna)
2. The length of the reinforcing steel (for a reinforcing steel segment centered directly beneath the antenna at fixed Z)
3. The rotation angle θ of the reinforcing steel in the XY plane (for a reinforcing steel segment centered directly beneath the antenna)
4. The tilt angle ϕ of the reinforcing steel in the YZ plane (for a long reinforcing steel bar centered directly beneath the antenna)
5. The length of the reinforcing steel gap (when one edge of the gap was centered directly beneath the antenna)
6. The lateral location of the reinforcing steel gap (relative to the antenna center) when the gap was 1-in. wide

For measurements 1, 2, 5, and 6, the reinforcing steel bars were oriented parallel to the Y -axis.

As illustrated in Figure 18a and Figure 18b, the antenna housing was placed in a plastic mesh bag and suspended from the ceiling. Reinforcing steel bars were placed either on a Styrofoam table or supported by wooden side structures. For most measurements, there was ample distance between the antenna, the reinforcing steel, and the floor, to allow for relatively clean separation of the direct-coupled (DC) signal and the reinforcing steel and floor echoes. In none of these measurements was the antenna moving with respect to the reinforcing steel. Rather, with the geometry fixed, the researchers operated the equipment in “free running mode” to repeatedly fire GPR pulses and capture returning signals. Each captured signal was a 1024-point waveform spanning 8 or 10 nanoseconds of time and digitized using a 16-bit analog-to-digital (A-to-D) converter. For a given measurement setup, several hundred signals were averaged to remove electronic noise, after making small time adjustments to correct for equipment drift during the course of the measurements. In all cases, the researchers: (1) measured the GPR signal from the reinforcing steel target + support structure, (2) measured the GPR signal from the support structure alone (referred to here as the background signal), and (3) subtracted the two signals to estimate the GPR signal from the reinforcing steel target without supports. An example of background subtraction is illustrated in Figure 18c and Figure 18d for the case of a long reinforcing steel bar containing a 1-in. long gap. After background subtraction, the peak-to-peak voltage (V_{pp}) was used to quantify the strength of the reinforcing steel response (Eisenmann et al. 2016).

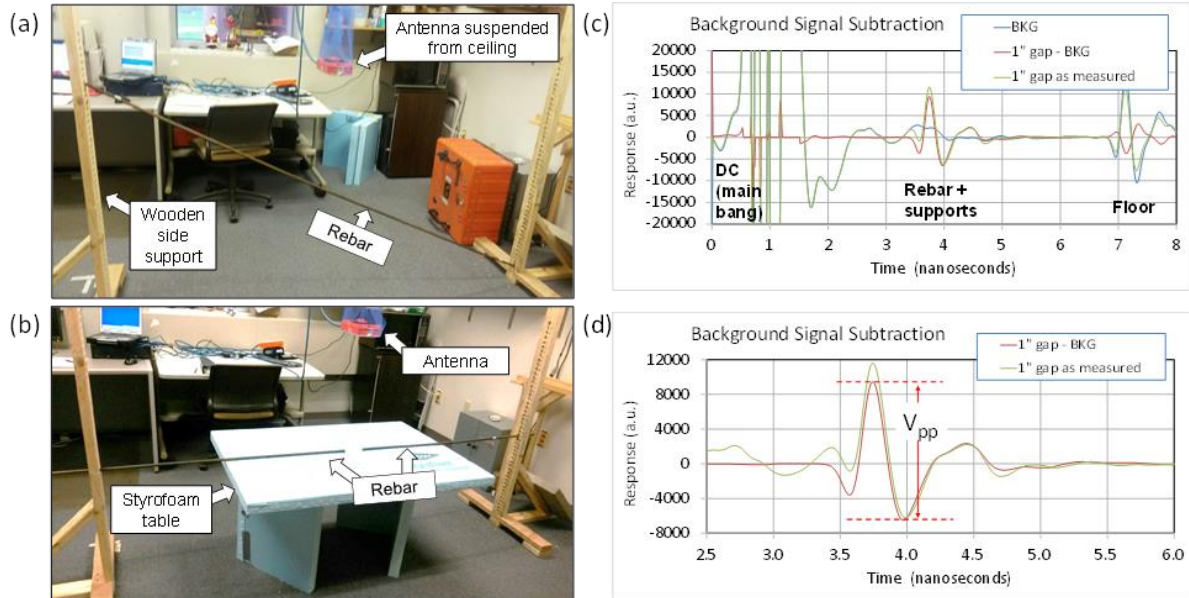


Figure 18. Examples of lab setups and of background signal subtraction for a long reinforcing steel bar containing a 1-in. gap

The results of these measurements are summarized in Figure 19 through Figure 24. Each figure has a similar format and depicts the measurement setup (a), examples of measured signals after background subtraction (b), and a graph of the dependence of the peak-to-peak reinforcing steel response on the quantity being varied (c).

The following points summarize the testing:

1. When the reinforcing steel depth Z was increased (Figure 19), the reinforcing steel response dropped steadily in amplitude and shifted later in time. The peak-to-peak response could be approximately summarized by the power $V_{pp} = C(Z+2.15)^{-1.65}$, where Z is the separation between the bottom of the antenna housing and the top of the reinforcing steel, and C is a constant depending on the gain setting used. In the power law, the researchers have modified the separation distance by adding an extra 2.15 in. They posited that $Z+2.15$ in. represented the distance of the reinforcing steel from an effective source location within the antenna housing. Without this modification, a power law representation (i.e., $C(Z)^p$) provides a much less accurate summary of the measured data.

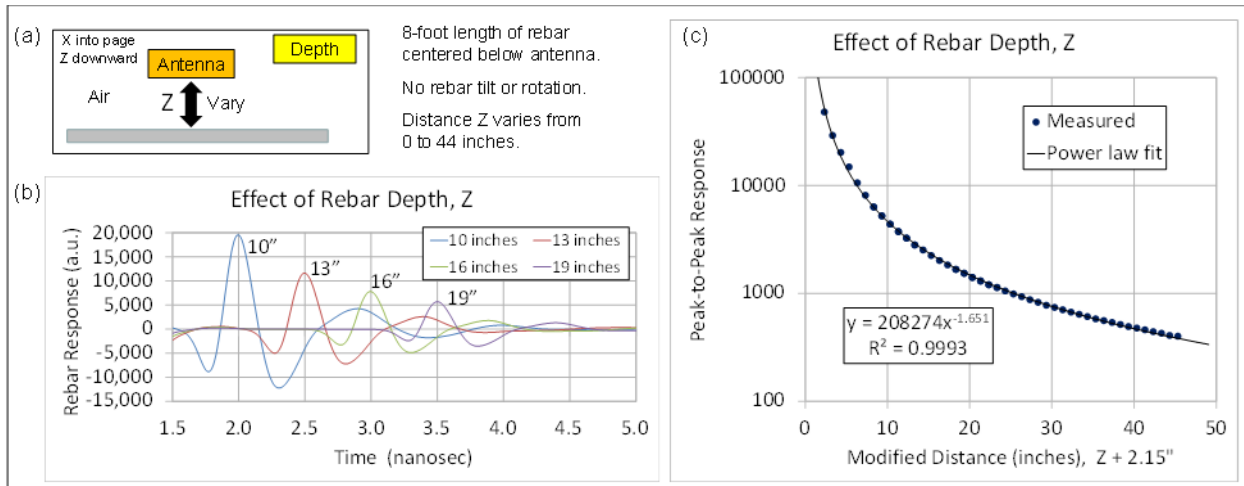


Figure 19. Effect of varying the reinforcing steel depth, Z

- When the reinforcing steel length L was varied (Figure 20), the arrival time of the GPR signal was relatively stable, but its amplitude and detailed appearance changed. The peak-to-peak response initially rose as L increased, peaking near L = 15 in. The response then fell, but beyond L = 36 in. little change was seen. The peak in the response was believed to be a consequence of net constructive interference from the sum of the reflected signals from metal surface elements distributed along the length of the reinforcing steel. A similar peak was predicted by a simple model. At the nominal center frequency (1.6 GHz), wavelength in air is $\lambda = 7.4$ in. Thus, the peak seen in Figure 20 occurs near $L = 2\lambda$, but that is coincidental since the peak length is also dependent on the standoff distance between the antenna and reinforcing steel (23.4 in. in Figure 20).

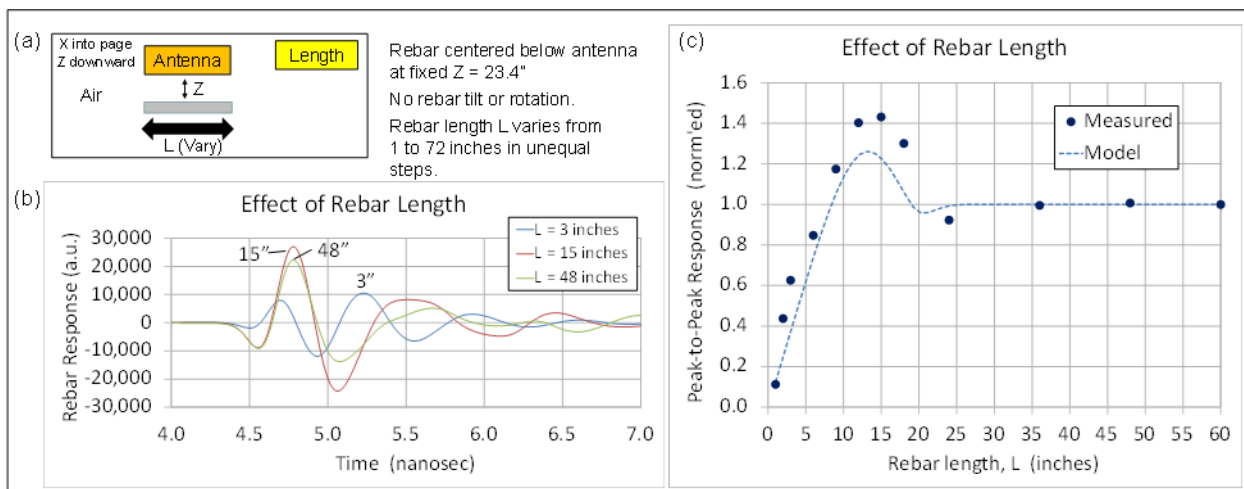


Figure 20. Effect of varying the reinforcing steel length, L

- When the reinforcing steel rotation angle (θ) was varied (Figure 21), the signal arrival time was quite stable, as expected, although the waveform shape varied slightly. As θ was increased from zero, the amplitude dropped steadily before stabilizing beyond about 60

degrees. Below 70 degrees, normalized plots of response versus angle were virtually identical for reinforcing steel segments of length 3, 12, and 60 in. In all three cases, the peak reinforcing steel response occurred at $\theta = 0$, where the electric field vector was polarized parallel to the reinforcing steel length.

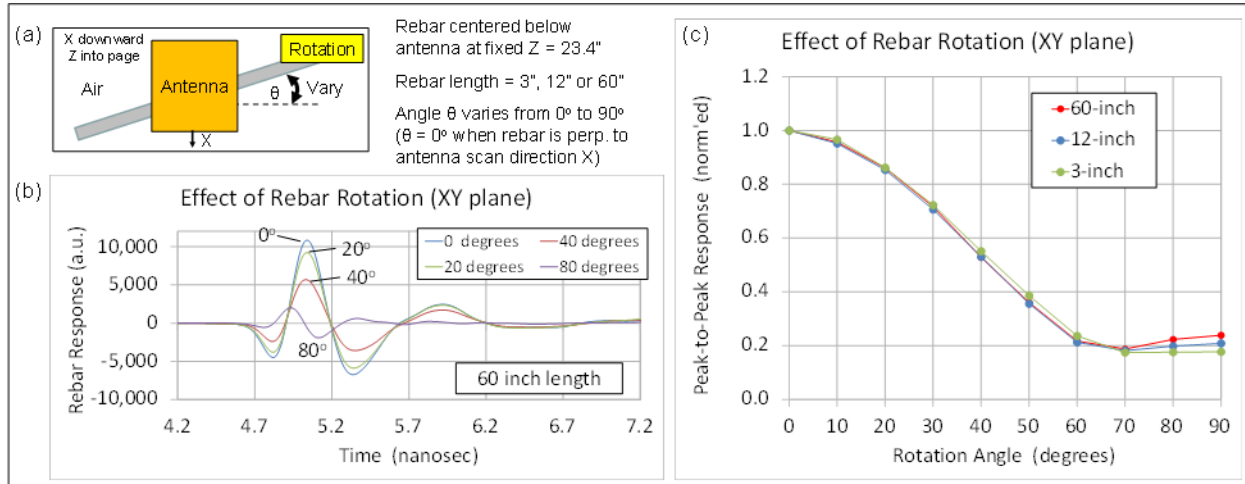


Figure 21. Effect of varying the reinforcing steel rotation angle θ

- In barrier rail inspections, reinforcing steel rotation and tilt angles were expected to be quite small ($<10^\circ$). For ease in performing the tilt measurements, the tilt angle was only varied from 0 to 25 degrees (Figure 22). Within this range, the reinforcing steel response dropped slowly in amplitude and shifted to the left in time as ϕ increased. The time shift was evidently due to the shortening of minimum distance (D) between the reinforcing steel and antenna when the vertical separation (Z) was held constant and the tilt angle increased (Figure 22a). Figure 19 shows that shortening the distance from the reinforcing steel to the antenna increased the reinforcing steel response. The researchers attempted to correct the data of Figure 22 for this effect, i.e., to show how the peak-to-peak amplitude would likely depend on ϕ if the distance D were held fixed at 23.8 in. First, the signal arrival time information was used to compute D as a function of tilt angle. Then, the signal amplitude was corrected for this change in depth using the power law of Figure 19c (assuming that the law applied similarly to both un-tilted and tilted reinforcing steel). Corrected and uncorrected data were compared in Figure 22c. It appeared that the correction had little impact below 5° tilt, but acted to nearly double the percentage signal loss due to reinforcing steel tilt at the higher angles.

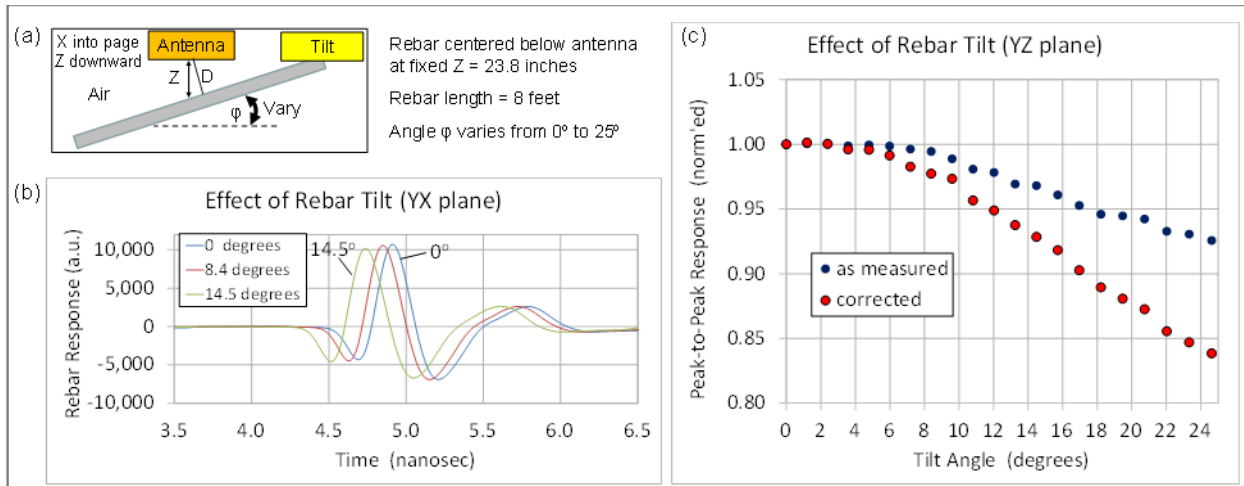


Figure 22. Effect of varying the reinforcing steel tilt angle ϕ

- In Figure 23, the gap (G) between two long reinforcing steel segments was varied, with one edge of the gap always located directly below the center of the antenna housing. The reinforcing steel response was stable in time and shape but dropped in amplitude until the gap reached 8 in. For larger gaps, the normalized response appeared to be approaching 0.5 as expected. Note that for a very large gap, half of the reinforcing steel was effectively present beneath the antenna, and the other half was too far away to return a response within the time window in question. Thus, the measured response for a large gap was expected to be one-half that of a long intact reinforcing steel bar.

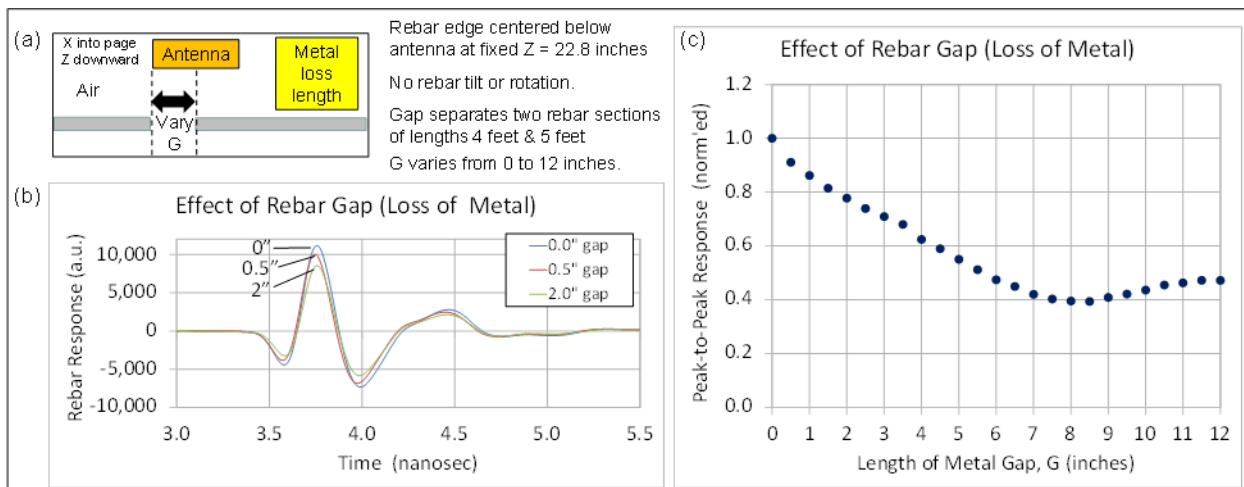


Figure 23. Effect of varying the reinforcing steel gap length G

- In Figure 24, the reinforcing steel gap was fixed at 1.0 in., but the lateral location of the gap was varied. This configuration is particularly germane to barrier rail inspection since the region of corrosive metal loss will not be centered directly beneath the antenna due to geometric constraints. (See Figure 16.) When the 1-in. gap was introduced directly beneath the antenna, there was a 13% reduction in response relative to an intact reinforcing steel

segment. As the gap center moved away from the antenna, the reinforcing steel response eventually approached that of an intact reinforcing steel bar (no gap) as expected. However, a response peak was observed when the gap center was located about 8 in. (or about one EM wavelength) laterally from the antenna center. At this peak, the reinforcing steel response was about 15% higher than that of an intact reinforcing steel. Similar to Figure 20, the response peak seen in Figure 24 was believed to be a consequence of net constructive interference from the sum of the reflected signals from metal surface elements distributed along the lengths of the two reinforcing steel segments bracketing the gap.

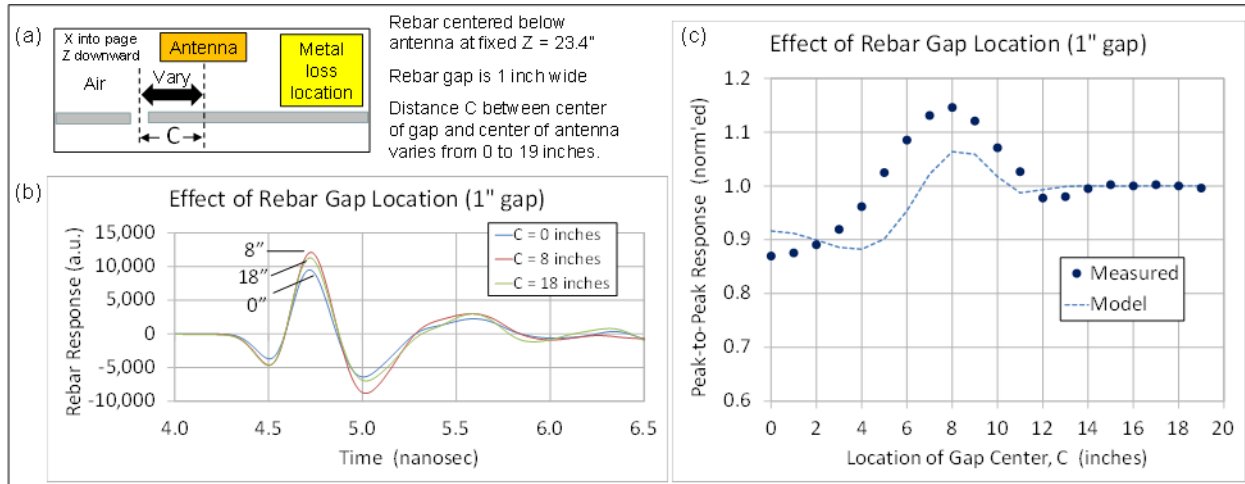


Figure 24. For a 1-in. reinforcing steel gap, effect of varying the gap location C

These observations have important consequences for corrosion detection. Recall that the approach described in Figure 1 was based on two assumptions: (1) corrosive thinning will reduce the amplitude of the reinforcing steel signal and (2) there will be a larger signal reduction if the antenna is located closer to the thinned region. Figure 24c illustrates that the second assumption need not be true. There are clearly situations where a larger response can be measured from a reinforcing steel bar with missing metal than from an intact reinforcing steel. Thus, care must be exercised when choosing the two vertical measurements positions (antenna on-the-roadbed and antenna elevated) used during bridge inspection.

Laboratory Measurements in Solids: Effect of Reinforcing Steel Position, Orientation, and Metal Loss on GPR Signals

In addition to the measurements and analyses of GPR data from the IA 210 bridge, the researchers continued the laboratory studies on the effects of various geometric factors on reinforcing steel signal strength. The peak amplitude of a reinforcing steel response can be affected by factors other than the total degree of metal loss, such as the depth of the reinforcing steel in concrete, the angular orientation of the reinforcing steel, and the location of the metal loss region relative to the antenna center. To develop a practical amplitude-based system for detecting corrosion-thinned reinforcing steel, it must be possible to assess and account for such factors. The researchers embarked on a laboratory study to systematically investigate the effects of certain geometric factors on the strengths of GPR signals reflected from reinforcing steel. This

section contains a discussion of efforts to move a step closer to investigating reinforcing steel embedded in concrete by surrounding the reinforcing steel with a powdered material having similar GPR properties to concrete. In Eisenmann et al. (2013), damp sand seemed to work best of the various powders that were investigated. When the moisture level of the sand was set near 5.4% by weight, the speeds of EM waves in sand and concrete patio blocks were found to be similar and echoes from sand/concrete interfaces were small.

These latest laboratory measurements consequently used moist sand as a “phantom” for concrete in much the same way that medical phantoms are used in place of tissues and organs in some ultrasound research. The setup used is shown in Figure 25.

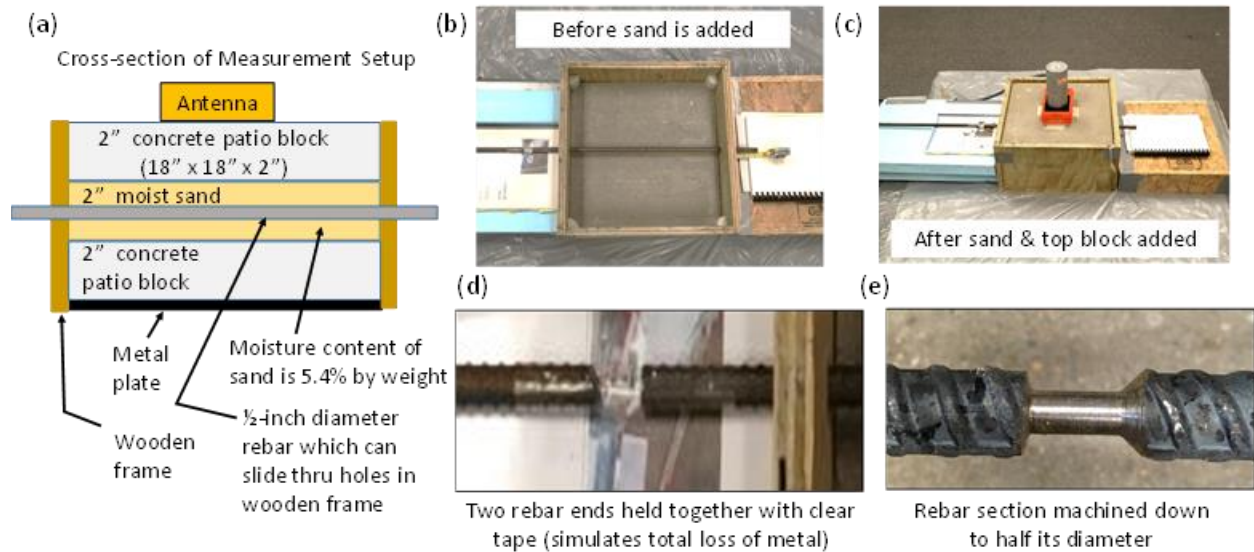


Figure 25. Reinforcing steel-in-concrete-phantom measurement details: (a) laboratory setup, (b) and (c) reinforcing steel in wooden frame before and after moist sand added, and (d) and (e) reinforcing steel targets used to simulate loss of metal due to corrosion

A wooden frame provided lateral support for a 2-in. thick sand layer that is sandwiched between two 2-in. thick concrete patio blocks. Plastic vertical spacers (not shown) were placed into the four corners of the frame in between the patio blocks and served to hold the patio blocks 2.0 in. apart. With a reinforcing steel target in place in the box, sand was added until the volume between the patio blocks was fully filled. Two 0.5-in. diameter holes drilled into the wooden frame allowed the reinforcing steel to slide through the sand layer. Two methods were used to simulate reinforcing steel thinning (metal loss) due to corrosion. In the first method (Figure 25d), a gap was introduced in the reinforcing steel metal by fastening together two parallel reinforcing steel lengths with their ends not touching. The ends were held a fixed distance apart using either clear plastic tape (Figure 25d) or a thin cardboard sleeve. In the second method (Figure 25e), a lathe was used to remove metal from a section of the reinforcing steel, thus reducing its diameter. For either method, the reinforcing steel assembly was pulled through the sand layer to study the dependence of the reinforcing steel response on the location of the thinned region. The GPR antenna housing was typically fixed in position on the upper concrete block, and held in place

with a top weight. A thin metal plate located under the bottommost patio block provided a strong, easily observed GPR signal arriving well after the reinforcing steel signal of interest.

In the “reinforcing steel in air” measurements discussed in Eisenmann et al. 2013, six setups were used to allow the GPR reinforcing steel response to be studied while a single key geometric parameter was varied. These parameters were as follows:

1. Distance from the antenna to the reinforcing steel (“depth”)
2. Total length of the reinforcing steel segment
3. Reinforcing steel rotation angle in the plane of the antenna housing
4. Reinforcing steel tilt angle in an orthogonal plane
5. Length of the reinforcing steel gap when a gap is present
6. Lateral location of the reinforcing steel gap relative to the antenna center

Similar sensitivity studies were planned using “reinforcing steel in sand” setups. Preliminary measurements were made for categories (3) and (6) using either the 1.6 GHz or 2.6 GHz antenna. These categories are particularly germane to barrier rail inspections for two reasons: the reinforcing steel bars within the barrier rails are often slightly rotated from vertical, and the region thinned by corrosion generally will not pass directly under the center of the antenna for a scan conducted along the roadbed.

To investigate the effect of minor rotation angles on reinforcing steel responses, a 4-ft long intact reinforcing steel segment was centered in the test fixture of Figure 25, and the 2.6 GHz antenna housing was then rotated in increments of 5° from -25° to 25° . In practice, rotation angles for reinforcing steel in barrier rails were expected to be no more than 10° from vertical since angles of that order are easily recognized as errant by the human eye, allowing the angle to be corrected before concrete is poured. The results of the rotation angle study appear in Figure 26.

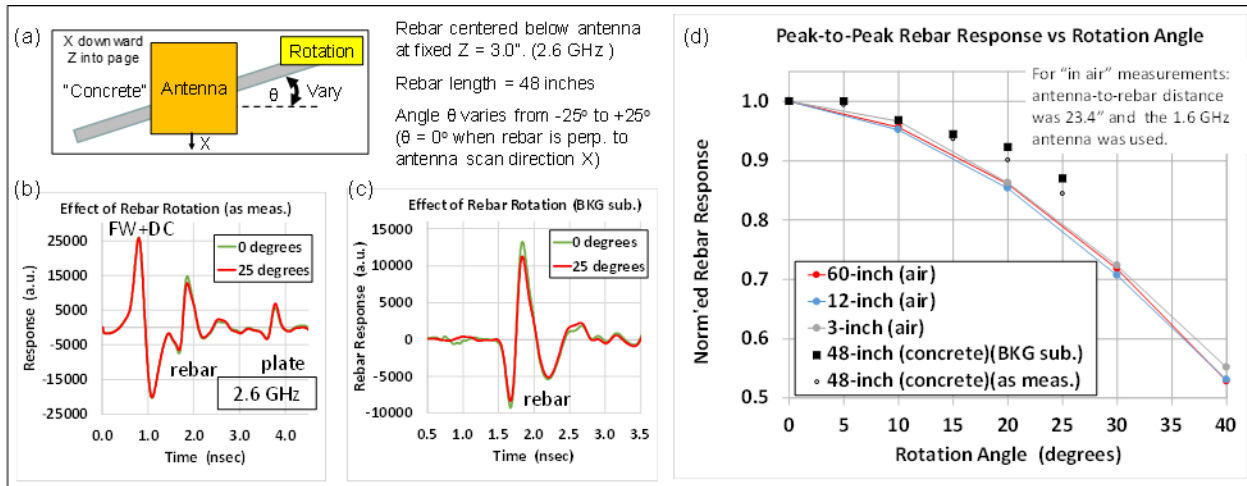


Figure 26. Effect of reinforcing steel rotation: (a) measurement setup, (b) representative GPR signals as measured, (c) reinforcing steel signals after background subtraction, and (d) dependence of peak-to-peak reinforcing steel amplitude on rotation angle, normalized to be unity at zero angle

Figure 26 and the other figures in this section show the data processing procedure described in Eisenmann et al. 2018. First, the raw GPR A-scan signal was measured with the reinforcing steel target positioned within the support structure. These raw A-scans, as shown in Figure 26b, contained three separate signals: (1) a combination of the FW echo and DC signal, with the latter resulting from direct flow of EM energy between the transmitting and receiving bow-tie antennas within the housing; (2) the echo from the reinforcing steel target; and (3) the echo from the metal plate. After all raw A-scans were acquired, the reinforcing steel target was completely removed from the fixture box, and a “background signal” was acquired. This background signal was then subtracted from each raw A-scan to obtain what may be termed the “reinforcing steel alone” response (unaffected by nearby interfaces). The procedure was not ideal since the void left by the reinforcing steel was not fully filled with packed sand. However, the subtraction process did remove most of the FW+DC signal, which overlapped with the beginning of the reinforcing steel signal. Thus, such background subtraction yielded a cleaner version of the reinforcing steel response, as illustrated in Figure 26c.

After background subtraction, the peak-to-peak amplitude of the reinforcing steel response was used as the primary measure of signal strength. The plate echo, which is not germane to the current study, was also affected by background subtraction. If the reinforcing steel target was long and fully intact, then the plate echo approximately doubled in amplitude when the reinforcing steel was removed from the sand. Thus, in most cases, upon background subtraction, the plate echo was reduced in amplitude and flipped in phase. In the extreme case, where the reinforcing steel target had a very large gap with that gap centered under the antenna, the plate echo approximately vanished after background subtraction, since removal of the reinforcing steel target has little effect on the plate echo.

For the rotation angle study, peak-to-peak responses before and after background subtraction were plotted in Figure 26d, and compared with “reinforcing steel in air” results from Eisenmann

et al. (2013). In each case, the plotted points were averages over positive and negative angles. The earlier reinforcing steel in air studies used the 1.6 GHz antenna and three reinforcing steel bars of different lengths (3, 12, and 60 in.), all of which yielded very similar response-vs-angle curves for angles less than 70 degrees. For the current reinforcing steel in “concrete” study using 48-in. long reinforcing steel, a smaller angular range was considered and the response decline with increasing angle was found to be slightly smaller than that seen in air. This may be associated with the change in the antenna center frequency from 1.6 GHz (air) to 2.6 GHz (concrete). Similar reinforcing steel in concrete measurements at 1.6 GHz are planned in the future. Figure 26 shows that the reinforcing steel in concrete response is reduced by less than 3% for rotation angles of less than 10 degrees, boding well for practical applications.

The effect of reinforcing steel metal loss on GPR responses was of considerably more interest in barrier wall applications. Both the total degree of loss and the location of the loss region relative to the antenna were of importance. New reinforcing steel in concrete measurements to address such effects appear in Figure 27 and Figure 28. Both figures follow a similar pattern; (a) depicts the measurement setup; (b) depicts the representative reinforcing steel signals after background subtraction for the 2.6 GHz antenna; and (c) depicts the dependence of peak-to-peak reinforcing steel amplitude on gap location and offset distance, respectively.

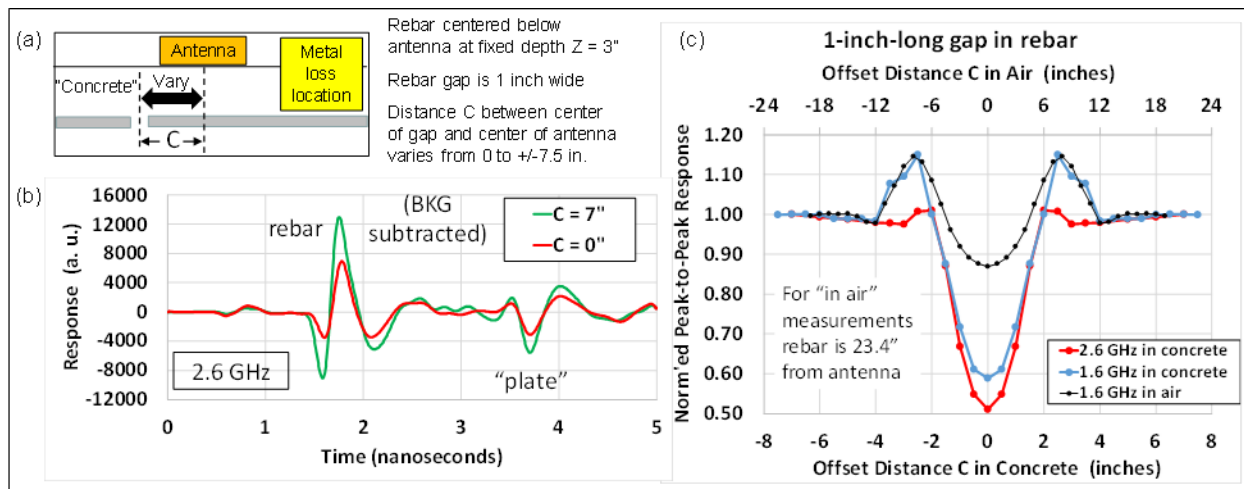


Figure 27. Effect of varying the gap location C for a 1-in. reinforcing steel gap

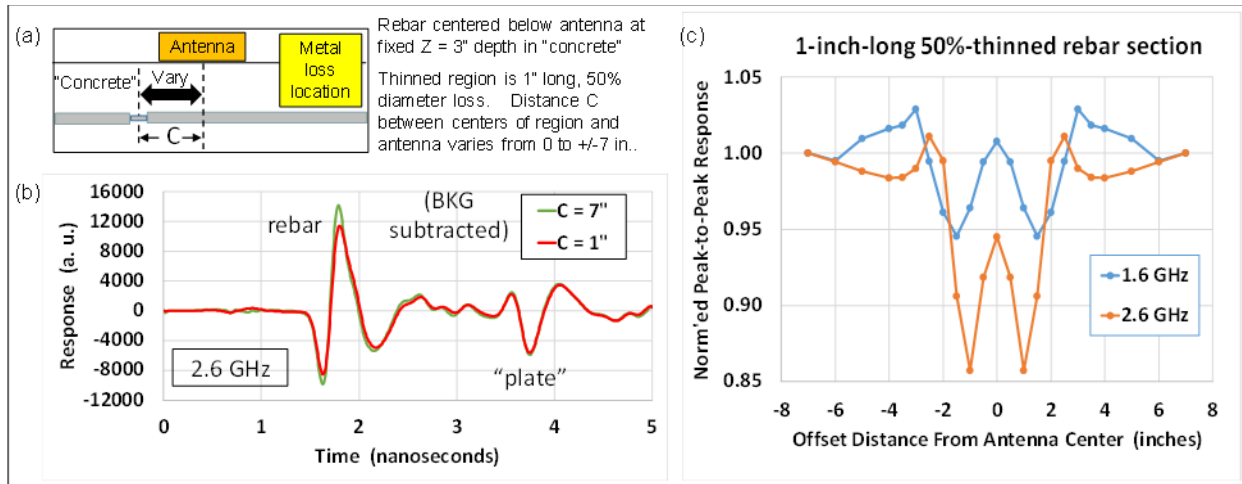


Figure 28. Effect of varying the offset distance C for a 1-in. long, 50%-thinned region

In Figure 27, the reinforcing steel target has a 1-in. long gap of missing metal, while in Figure 28, the reinforcing steel diameter has been reduced by half over a 1-in. long segment. In each figure, the reinforcing steel response was displayed as a function of the lateral offset (C) from the center of the metal loss region to the center of the antenna. For both cases, similar measurements were made using the 1.6 GHz and 2.6 GHz antennas in turn. Background subtraction was used, and the data was symmetrized and normalized. For example, amplitudes measured at symmetric positive and negative offsets were averaged and replotted at both positive and negative offsets. All amplitudes were normalized to unity when the lateral offset C is large (typically near 7 in. in concrete).

For the 1-in. gap case (Figure 27), the current in-concrete measurements were compared to previous in-air measurements, which were collected using only the 1.6 GHz antenna. For both the in-air and in-concrete measurements of Figure 27, the reinforcing steel response was minimized when the gap was directly under the antenna. On either side of the central minimum, each curve displayed “horns” where the reinforcing steel response was actually larger than the response from a fully intact reinforcing steel bar (or from a gapped reinforcing steel bar with the gap located far from the antenna center). Such interference maximums were discussed in Eisenmann et al. (2016), and present a potential problem in practice since the presence of a gap can be missed in an inspection if the offset distance is improperly chosen. Note that a separate horizontal scale was used for offsets in the in-air results in Figure 27 that were associated with the much larger antenna-to-reinforcing steel distance for the in-air case. When the horizontal scale change was a factor of three, as shown in Figure 27c, the “horn” positions approximately align for the 1.6 GHz measurements in-air and in concrete. Overall, in Figure 27, for concrete the 2.6 GHz antenna was favored over the 1.6 GHz antenna for two reasons: (1) there was a larger drop in reinforcing steel response when the gap was centered under the antenna, and (2) the interference horns were much less pronounced.

For the 1-in. 50%-thinned case in Figure 28, the 2.6 GHz antenna was again favored for the same two reasons. Note, however, that the curves of the reinforcing steel bars response-versus-offset in Figure 28c were more complex in shape and did not attain their minima when the antenna was

directly over the thinned region. In practical barrier-rail inspections, this argues for scanning the antenna across rail sections at several different offsets relative to the cold joint to improve the chances of observing significant signal changes that indicate defective reinforcing steel.

These reinforcing steel in concrete measurements using the moist sand phantom were particularly good vehicles for undergraduate student research projects, allowing students to both earn scholastic credit hours and gain valuable experience in scientific research methods. The researchers plan to continue such studies as interested students make themselves available.

Ground Penetrating Bridge Results

A field trial of the GPR detection method was conducted at a bridge in central Iowa where IA 210 passes over I-35. The overpass spans about 200 ft and five 6-ft long sections were selected for study. Each section of road deck was scanned in two ways: (1) with the antenna carriage flush with the road deck and (2) with a (nominal) 2 x 4 in. wooden spacer placed between the antenna carriage and the road deck. The spacer served to elevate the antenna about an additional 1.5 in. above the road deck, and hence, 1.5 in. farther from the thinned reinforcing steel zone if thinning was present.

Field Measurements—Previous Experimental Work

Initial work began in order to inspect the barrier rail for evidence of reinforcing steel corrosion at the point where the barrier rail meets the bridge deck. Data collection from the 2012 field work is shown in Figure 29 and Figure 30.

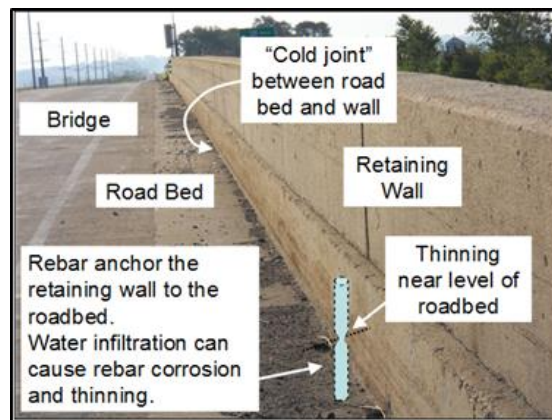


Figure 29. Identification of regions of interest on the bridge deck

In Figure 29, the region of interest was identified, along with the cold joint between the barrier rail and the bridge deck. In order to make a comparison of data collected at the mating point between the bridge deck and the barrier rail where it was believed that the greatest amount of corrosion occurred, a reference signal was obtained where it was believed that no corrosion would occur, approximately 1.5 in. above the bridge deck. Figure 30 shows the GPR unit during

the data collection in 2012, along with the GPR unit and the spacer used to elevate the GPR antenna above the perceived region of corrosion on the bridge deck.

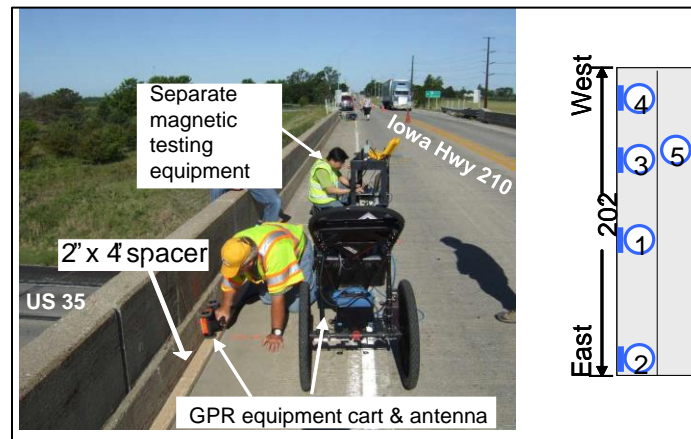


Figure 30. Data collection illustrating the spacer used in collection of the reference data

Based on the initial work performed in 2012 (Eisenmann et al. 2013), assumptions were made prior to data collection: corrosive thinning will reduce the amplitude of the reinforcing steel signal, and larger signal reduction will occur if the antenna is closer to the thinned region. After examination of the data collected in 2012 (illustrated in Figure 31), three regions of amplitude differences were identified in the two B-scans taken from one of the inspection sections of the bridge.

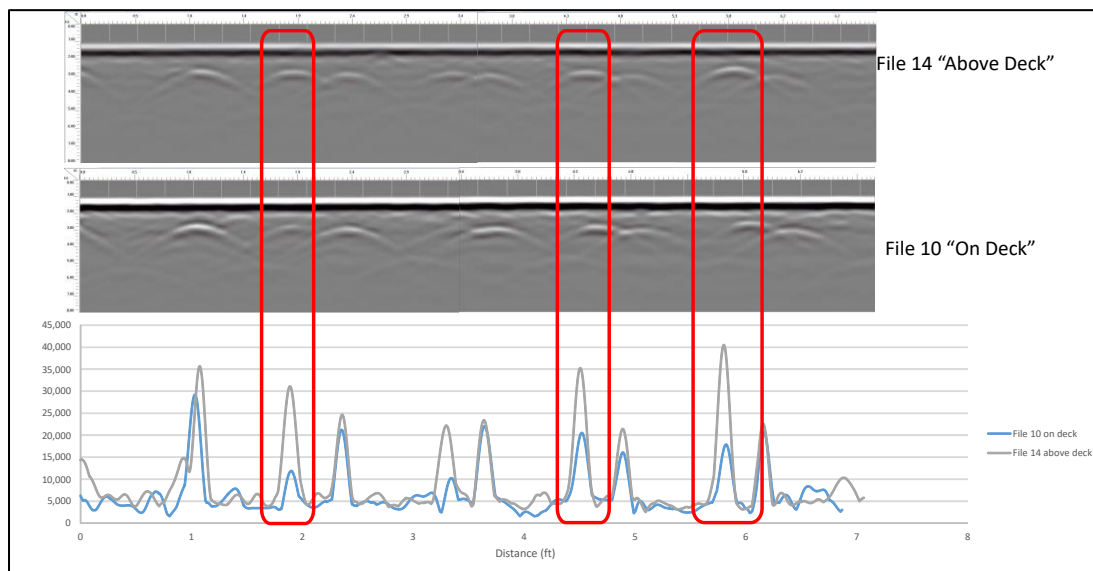


Figure 31. Example of B-scans and amplitude data take from a section of the bridge

The upper B-scan showed the data collected using a spacer, which placed the antenna 1.5 in. above the bridge deck. The lower B-scan illustrated the data collected with the antenna placed adjacent to the bridge deck. It should be noted that the GPR antenna was placed facing the

barrier rail, and moved parallel to the face of the bridge deck. The graph directly below the two B-scans shows the peak-to-peak amplitude of the signal received at the point of the hyperbola taken directly from the reinforcing steel bar located within the barrier rail. The peaks of higher amplitude in the graph were taken from the position defined as above deck and the lesser amplitude peaks were taken from the B-scan where the data were collected on deck. This example shows that the initial assumptions were believed to be correct.

The responses from the reinforcing steel data from all of the scans were processed and plotted onto one graph, as shown in Figure 32.

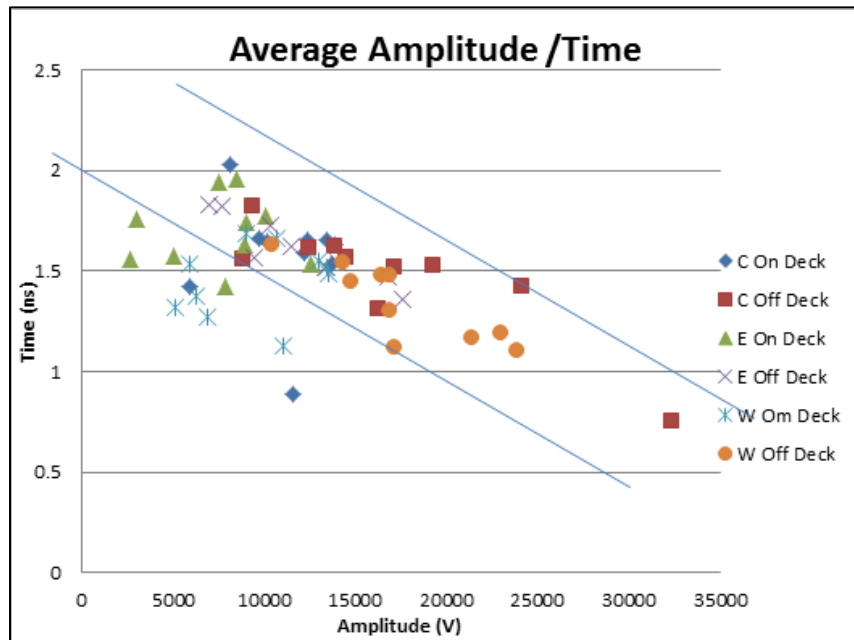


Figure 32. Compilation of data collected in 2012 from all inspected sections

The data showed a nominal trend where the lower amplitude obtained from the reinforcing steel tended to occur with a longer time of arrival, and for those reinforcing steel bars where the signal amplitude was greater, the time of arrival was shorter. From the plotted data in Figure 32, it appears that there were a dozen “thinned reinforcing steel” segments, where the reinforcing steel had an unexpectedly low amplitude relative to the signal arrival time. These points were believed to be regions where the reinforcing steel had thinned due to unwanted corrosion of the metal (Jensen et al. 2013).

GPR Field Measurements—Recent Experimental Work

Five years after the initial data were gathered from the barrier rails on this particular bridge, data were collected again at approximately the same locations. The method of collection was slightly different for the recent field data because the conditions on the surface of the bridge deck had changed. The bridge was scheduled for resurfacing, thereby exposing the joint between the barrier rail and the original bridge sub-deck. This circumstance allowed for a comparison of

three different positions of the antenna on the barrier rail: the on deck position, the above deck position (both previously recorded), and on the cold joint position. All three antenna positions are shown in Figure 33.

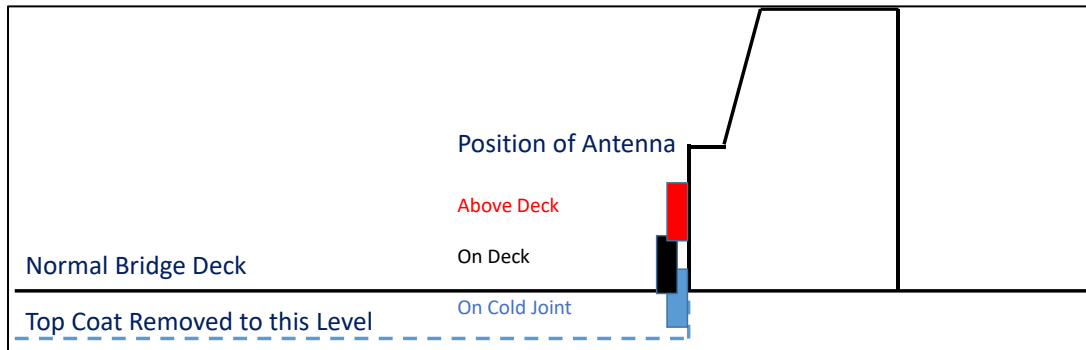


Figure 33. New antenna positions for data collection

An additional issue with this data collection was that fact that the missing top surface of the bridge deck made the method of positioning the antennas a bit more challenging when trying to collect data from the previous positions. Figure 34 through Figure 36 show several different perspectives of the bridge condition during the 2017 inspection.



Figure 34. Gap shown in the bridge deck near an inspection site



Figure 35. Amount of concrete removed during initial repair efforts



Figure 36. Configuration of material used to elevate the antenna to mimic the 2012 inspection location

Figure 37 displays three separate B-scans from one of the sections. Three reinforcing steel segments, identified within Figure 37, show the differences in amplitude, likely due to corrosion over time. At the cold joint, the echo from the reinforcing steel is virtually non-existent when compared to the echoes from the on-the-deck and the above-the-deck locations. SAFT was performed on the scans to further illustrate the differences between the amplitudes of the three B-scans.

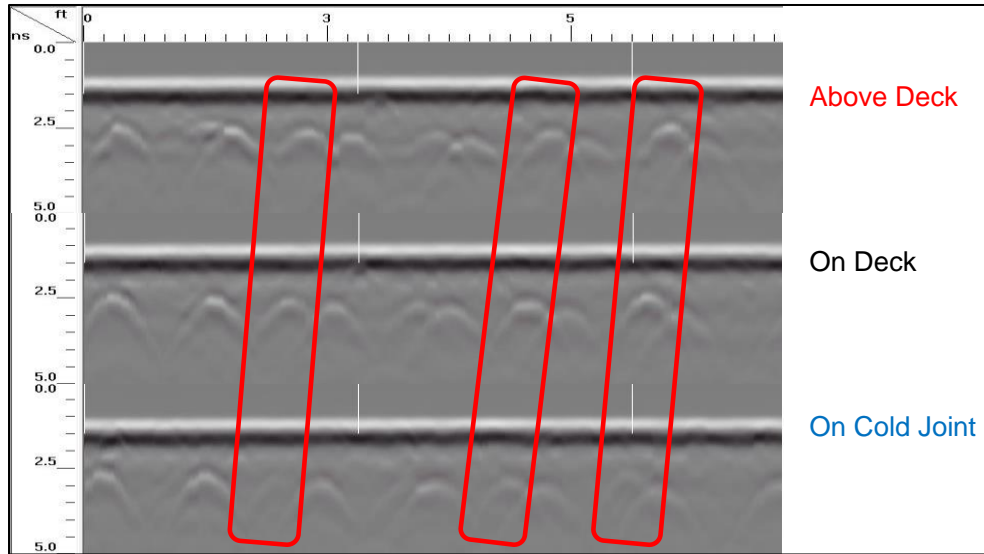


Figure 37. Example of data collected on three different levels

Figure 38 displays the hyperbola from the original data scans that have been reduced to points of intensity. By performing SAFT on the data, in addition to reducing the hyperbola to points, the overlap that occurred from reinforcing steel bars that are in close proximity to one another was separated and more easily identified. It was apparent in looking at the reinforcing steel overlap from Figure 37 that the separation of the different reinforcing steel bars could be somewhat difficult. Additionally, when quantifying the amplitude of each reinforcing steel reflection, the method used to quantify the data became easier.

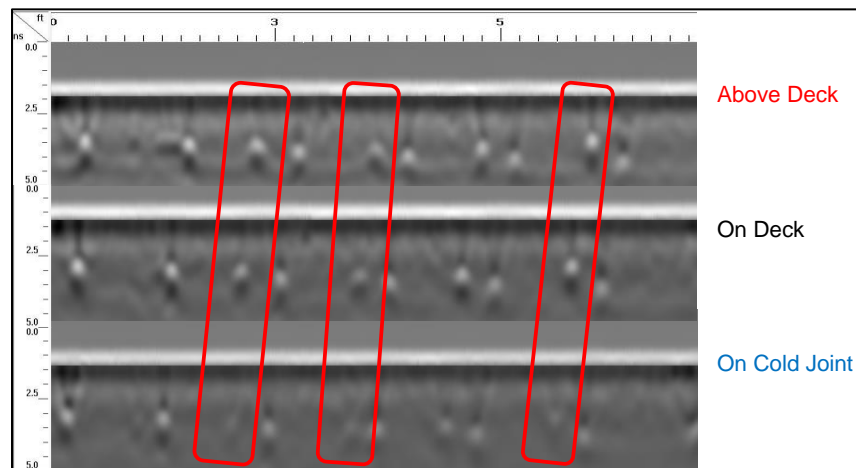


Figure 38. Same data with SAFT performed

Finally, after performing SAFT on the data from 2012 and 2017, the amplitude of the response versus the time of return of the signal onto one plot was plotted. Figure 39 shows similar trends to those seen in Figure 32, with points falling below the trend line, indicating probable material loss due to corrosion. (Files 10 and 14 in the plot are from 2012, and the remainder of the files are from the 2017 data collection.)

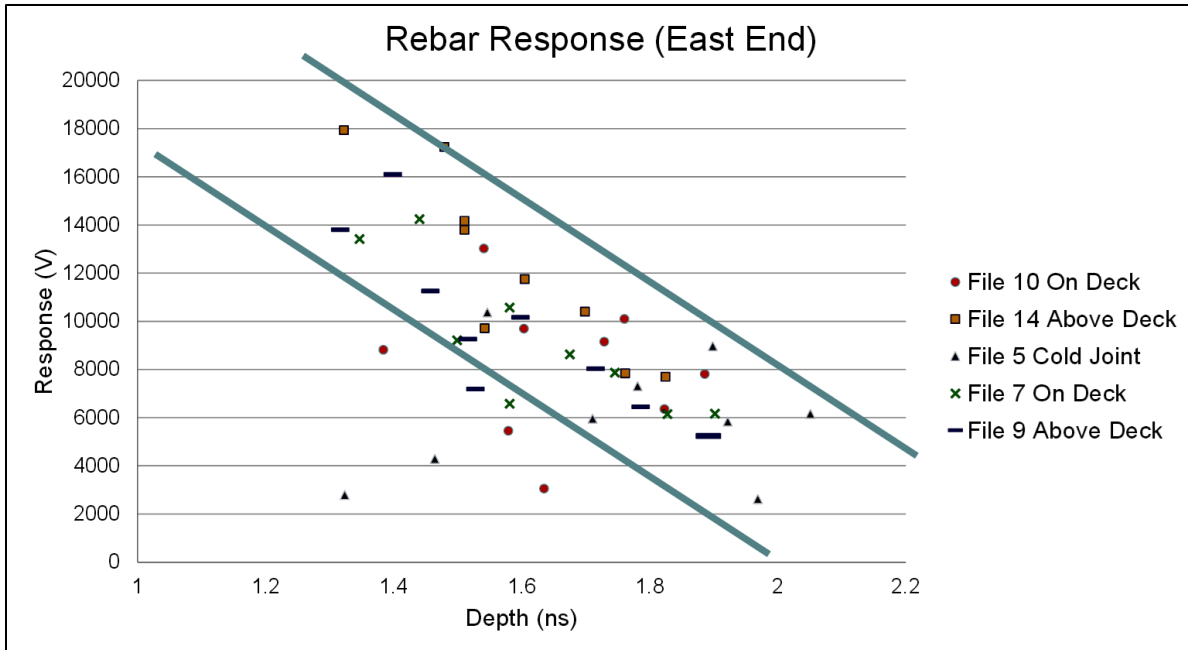


Figure 39. Combined data from one section showing both field dates

As anticipated from the earlier field work in combination with the laboratory work, several of the signals taken from the cold joint were much lower than signals taken from the on-the-deck” or above-the-deck signals. In order to verify the difference in signals, the final step was to physically remove the concrete from the suspect reinforcing steel and verify the remaining amount of reinforcing steel material present.

Figure 40 through Figure 42 are the results of the data collection efforts for three separate time periods, June 2012, December 2016, and June 2017, respectively. The results from 2012 (Figure 40) were discussed earlier in this report, and are shown here for comparison only. In Figure 41 (December 2017), there were similar results to those of the 2012 data. Conditions for this collection date were not optimal, with temperatures around 35°F to 38°F, with damp conditions on the concrete as a result of melting snow. It should be noted that even with the poorer climate conditions, the trend for the data collection was similar to that of the 2012 data. The last data collection results, in Figure 42, again show similar results to those of 2012 and 2017. As in the images of Figure 34 through Figure 36, while the climate conditions were better for data collection, the physical conditions for data collection were not ideal, yet similar trends were noted.

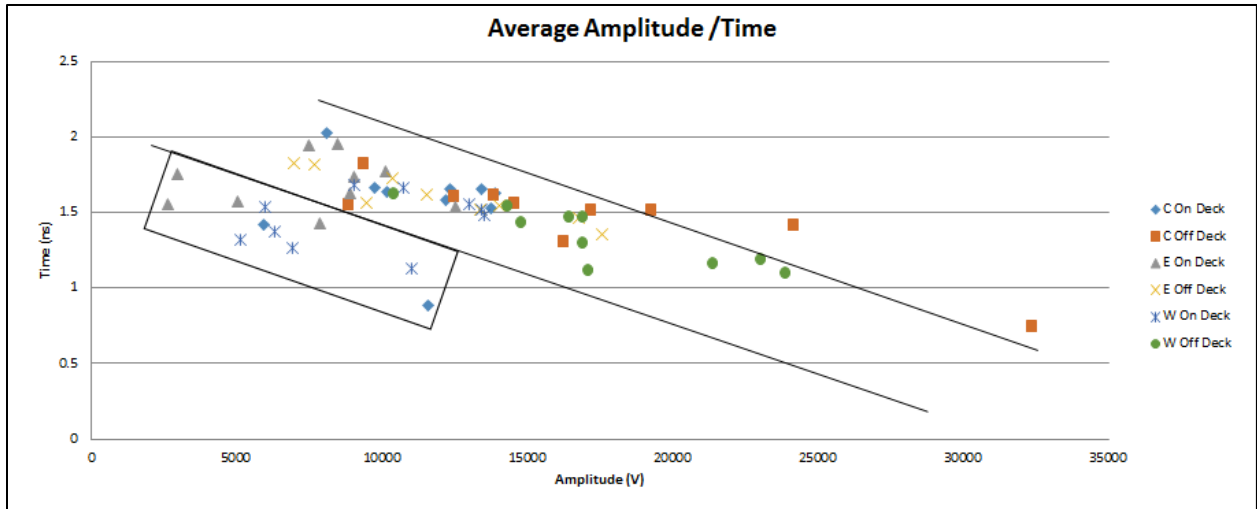


Figure 40. Data collection from June 2012

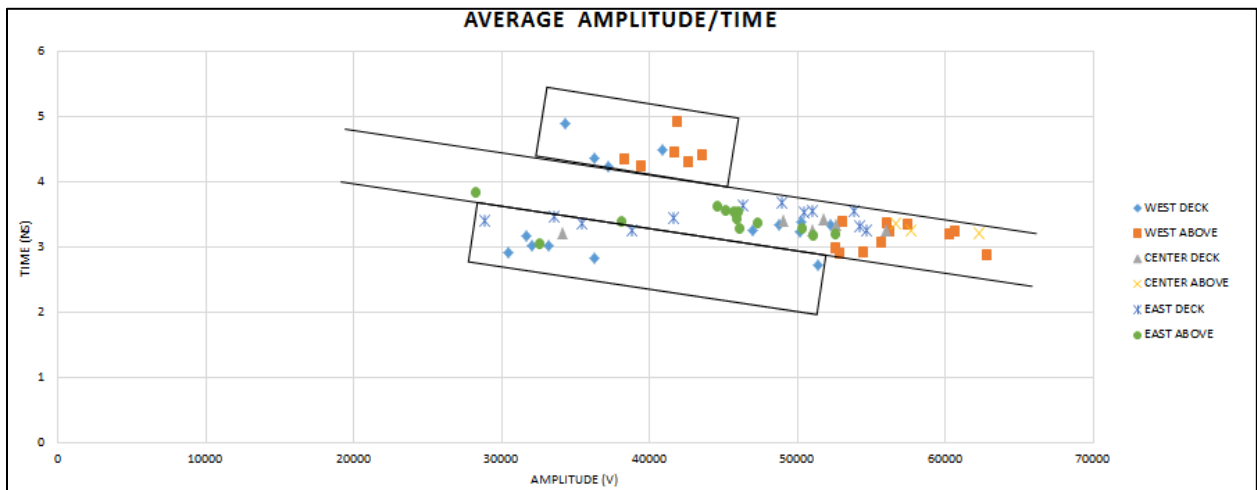


Figure 41. Data collection from December 2016

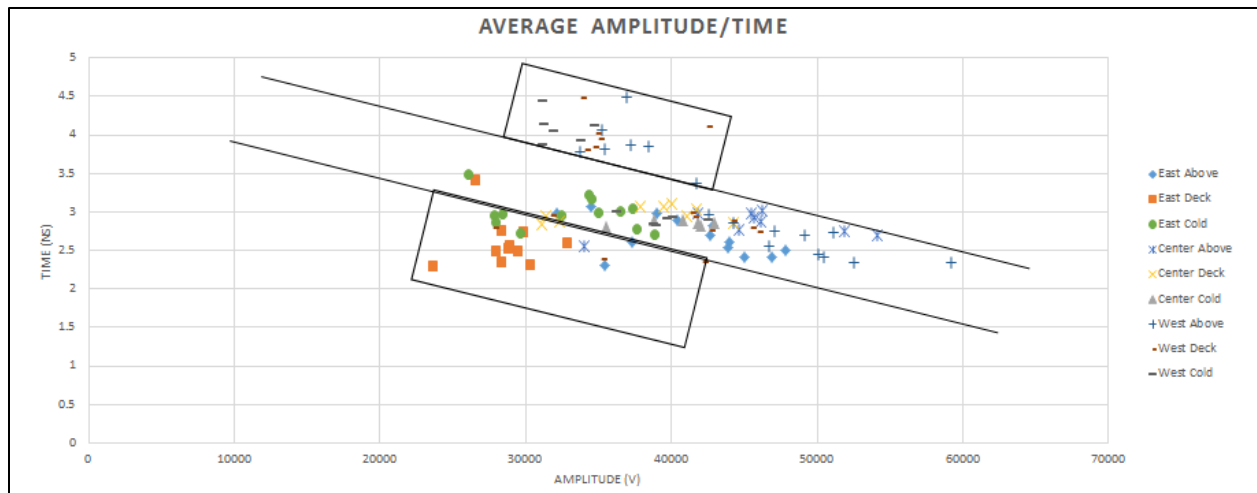


Figure 42. Data collection from June 2017

Figure 42 reveals the answer to some questions, but raises others. All of the graphs have a low outlier group, and when looking at Figure 40, there is no high outlier group. It was also found that if a reinforcing steel bar was in either outlier group, it was not also in the main trend or in the opposite outlier group. This validated the data due to the results not being contradicted from each subgroup of reinforcing steel. With the high outlier group only showing up in the December 2016 and June 2017 data, it was theorized the high outlier groups were the remnants of the main trend group from the June 2012 data. After five years, more corrosion occurred on most, if not all, of the reinforcing steel. This made almost all of the reinforcing steel (besides the high outlier groups) show material loss, causing the reinforcing steel bars that were already in the lower outlying group in June 2012 to become even more corroded, therefore, remaining as the low outlier group.

The original intent of this phase of the research was to validate the condition of the reinforcing steel, matching it to the amplitude of the GPR signal. A gap in communications between the bridge repair company and the researchers resulted in the original reinforcing steel being discarded before it could be inspected. Because of this communications gap, all of the important reinforcing steel information comprising the research base was lost. The researchers were then able to obtain some of the reinforcing steel from the north barrier rail of the IA 210 bridge. These sites were not inspected due to the condition of the concrete on the face of the barrier rail, but they did allow for examining the condition of the reinforcing steel based on its location in the barrier rail.

Figure 43 shows the reinforcing steel bars as numbers 1 through 6 left to right, and going from east to west. The east reinforcing steel is closer to the end of the bridge and the respective drain, where most of the water flows during runoff, allowing more moisture and corrosive substances to get into the cold joint, which causes corrosion to occur. The reinforcing steel bars closer to the west were closer to the center of the bridge, allowing less water flow into the cold joint, resulting in less corrosion.

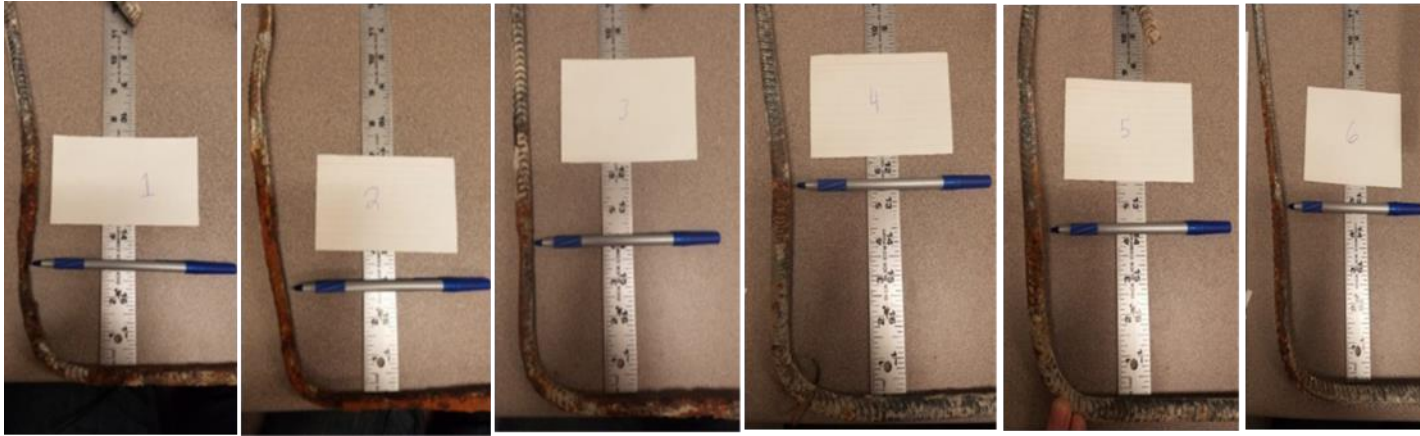


Figure 43. Reinforcing steel taken from IA 210 bridge after demolition of part of the bridge

Having the reinforcing steel segments in hand allowed the researchers to calculate the material loss. Measurements were made from a non-corroded part of each reinforcing steel bar, along with a measurement of the most corroded portion of the reinforcing steel, which was at the point of the cold joint. In Figure 43, the tip of the pen points to where the most corrosion occurred on the reinforcing steel. Figure 44 shows the material loss percentage that came from the reinforcing steel. The amount of material loss varied from approximately 60% on the location nearest the drain to approximately 5% at a point where the reinforcing steel was farthest from the drain.

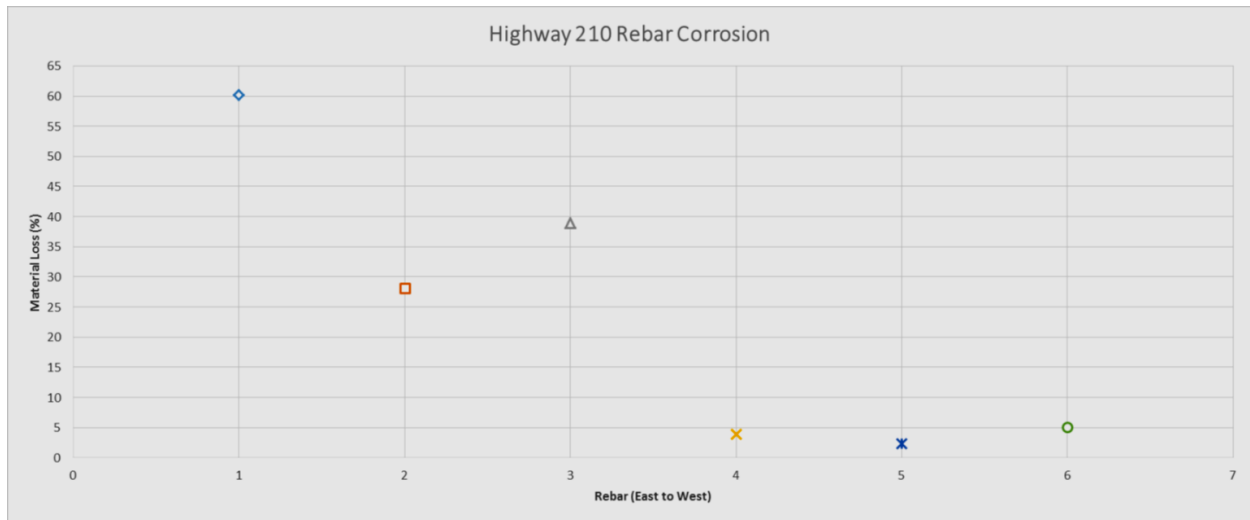


Figure 44. Material loss due to corrosion from reinforcing steel in Figure 43

Electromagnetic Testing

Electromagnetic Laboratory Results

For this study, the researchers attempted to use a MFL system (similar to what was used in the Phase I project) to detect material loss in reinforcing steel. Unfortunately, the individual who had the expertise in this measurement system was no longer available to participate in the study, but attempts were made to replicate the system and the work.

The plan for this work followed similar steps as Phase I: (1) laboratory work trying to detect material loss on bare reinforcing steel, (2) detection of material loss in the mock-up samples created in Phase I, and (3) field trials on the barrier rail itself.

The MFL scanning system recreated and shown in Figure 45 consisted of a power supply, a function generator, and an electromagnetic yoke that produced a magnetic field. The magnetic flux leakage, which occurs due to loss of material, was measured with GMR sensors, which are sensitive to changes in electrical resistance.

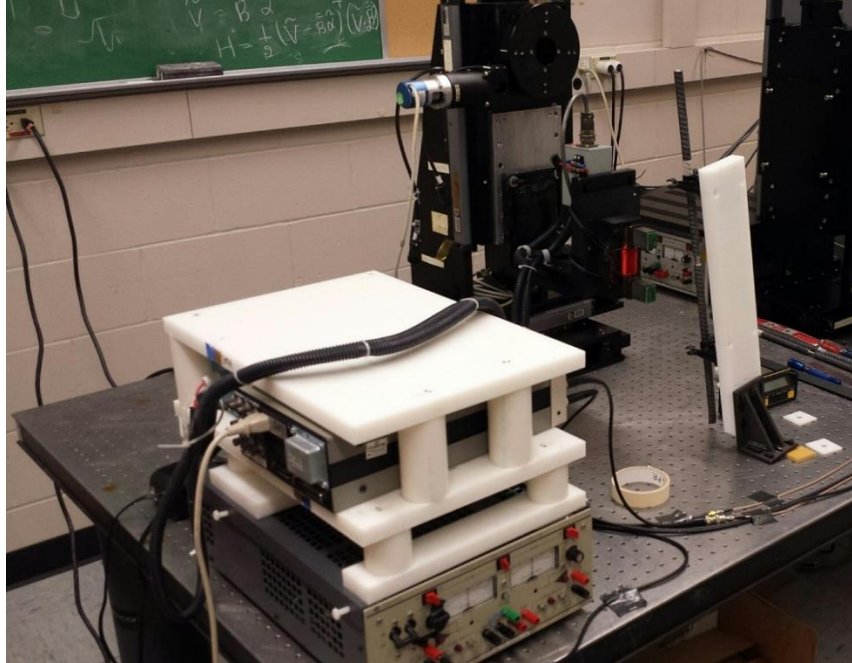


Figure 45. Reconstructed MFL system

Three bare, 24-in. long #4 reinforcing steel bars with a nominal diameter of 0.5 in. were used in Stage 1 of the feasibility study (Figure 46a). Two of three bars, R-2 and R-3 as shown in the figure, were machined to create artificial defects that correspond to approximately 25% and 50% material loss, respectively.



Figure 46. (a) Bare #4 reinforcing steel samples and (b) mockup samples consisting of either #4 or epoxy-coated #6 reinforcing steel bars

The diameter and length of the defects are shown in Table 2.

Table 2. Dimensions of the artificial defects in bare #4 reinforcing steel bars shown in Figure 46a

Reinforcing steel sample	Diameter D	Length L
R-2 (25% loss)	0.37 in.	0.555 in.
R-3 (50% loss)	0.25 in.	0.533 in.

Five mockup samples prepared in this project were used in the Stage 2 study (Figure 45b). Three samples consisted of #4 reinforcing steel bars, two of which were machined to produce 25% and 50% material loss. The other two mockups have epoxy-coated #6 reinforcing steels, one of which was machined to simulate a 50% material loss. The reinforcing steel bar size and the amount of material loss appear in Table 3 (Jensen et al. 2013).

Table 3. List of mockup concrete samples (Figure 46b) used in the Stage 2 study

Sample	M1	M2	M3	M4	M5
Reinforcing steel	#4 [†]	#4	#4	#6	#6
Material loss	0%	25%	50%	0%	50%

[†]Nominal diameter = 0.5 in. (12.7 mm)

The experimental setup for the laboratory MFL studies is shown in Figure 47a. The sensor probe (Figure 47b) consisted of a c-core electromagnet made of ferrite, which was driven using a bipolar power amplifier (Model: BOP 20-20, Kepco, Inc.) to apply a low frequency (20 Hz) sinusoidal magnetizing field to reinforcing steel samples. Two commercial GMR sensors (Model: AAH002, NVE, Corp) were mounted on the pole pieces to detect the magnetic field in the vertical direction. GMR sensors were used as they offer substantially higher sensitivity readings than Hall effect sensors. Nevertheless, the GMR sensors have non-linear output characteristics (Figure 47c), rendering them more difficult to use than Hall effect sensors.

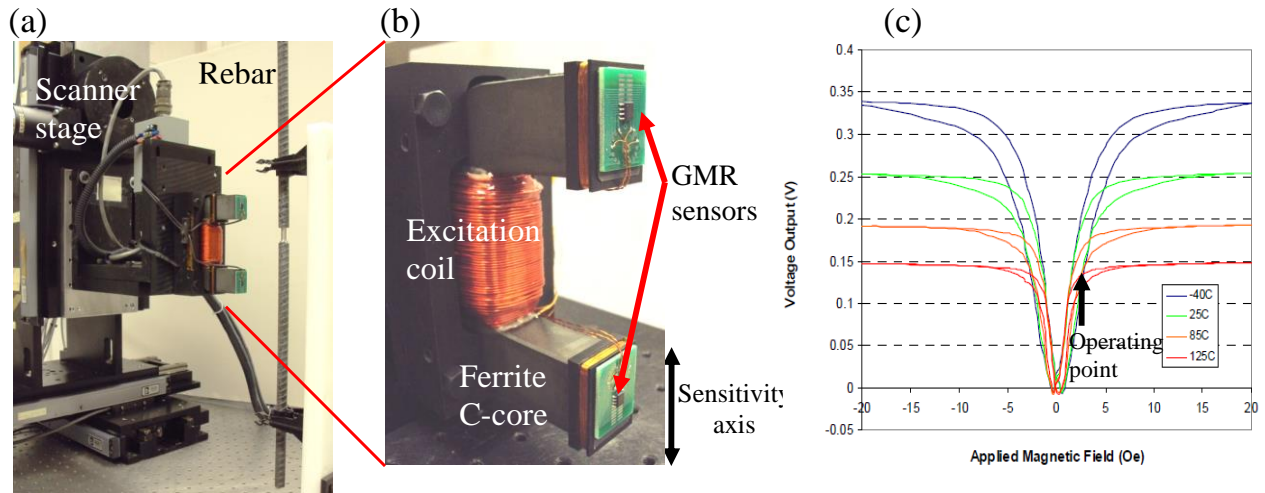


Figure 47. (a) Experimental setup for performing MFL scans on bare reinforcing steels and mockup samples, (b) close-up of MFL sensor probe consisting of an electromagnet to apply magnetizing field and two GMR sensors to detect the vertical component of leakage field at the pole-piece of the electromagnet, and (c) nominal output of the GMR sensors versus magnetic field

In particular, GMR sensors are axial sensors, meaning that they produce the same voltage output for both +ve or -ve fields. The sensor outputs also show hysteresis and become saturated at high fields, thus having a limited detectable field range that often varies inversely with the sensor sensitivity. In these measurements, a small direct current was applied to the electromagnet to produce a direct current biasing field. The goal was to set the operating point of the sensor close to the mid-point of the detectable field range (Figure 47c). For the laboratory studies of Stages 1 and 2, the MFL sensor probe was mounted on a three-axis scanner stage for performing line scans or raster scans over standalone reinforcing steels and mockup samples (Figure 47a). The outputs of the GMR sensors, which are typically in the order of 0.1 mV for reinforcing steels at a distance of 2.5 in., were detected using lock-in amplifiers (Model: 5210, EG&G, Princeton Applied Research) to obtain both the amplitude and phase (relative to the excitation signal) of the MFL signals. The signal amplitude was used in constructing line-scan profiles or C-scan images of MFL signals described in the following results section.

The parameters used for scanning during this phase of the research are listed below.

Scanning parameters:

A raster scan was done with different parameters that included step spacing (how frequently the data were recorded in the x direction), index spacing (how far the scanner moved in the z direction), and standoff distance (the distance between the reinforcing steel and the yoke).

In order to differentiate the different data files collected, a nomenclature was derived to differentiate among the files.

File Name Nomenclature:

- Each file was named for the following characteristics
 - Step and index size. Step is listed first in x direction. Index is listed second in z direction. (If only one value is used, only one number appears for x and z directions.)
 - Example: 10 mm x 10 mm z
 - Angle, if tilt 0 or 10 degrees
 - Example: 0deg
 - Standoff distance, the distance between the reinforcing steel and the yoke
 - Example: 2so means 2 in. between reinforcing steel and yoke
 - Material loss, how much material was removed from the reinforcing steel
 - Example: 25ml means 25% of the material was removed
- Example file name: 10x 10z 10deg 2so 50ml

MFL Measurements with Bear Reinforcing Steel

A difference in standoff distance can be seen in Figure 48 and Figure 49. Although the difference can be seen between material loss samples (25% versus 50%), the difference is not as easily detected when the distance between the sensors and the reinforcing steel is less.

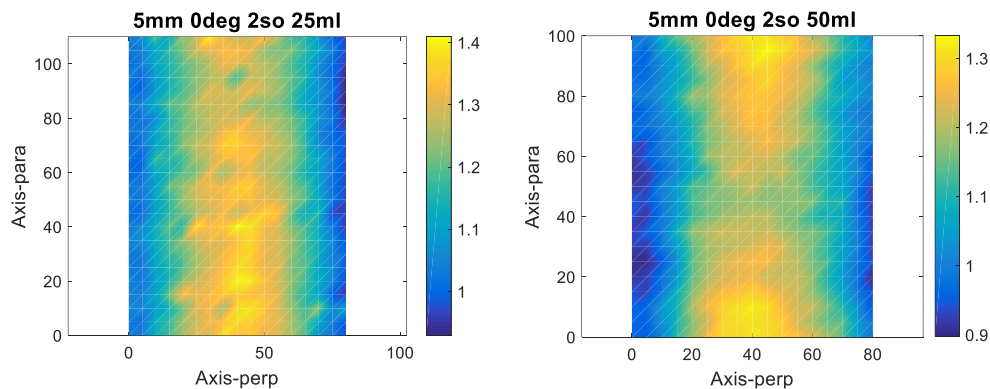


Figure 48. Difference in material loss between 25% (left) and 50% (right) material removal with a 2-in. standoff distance

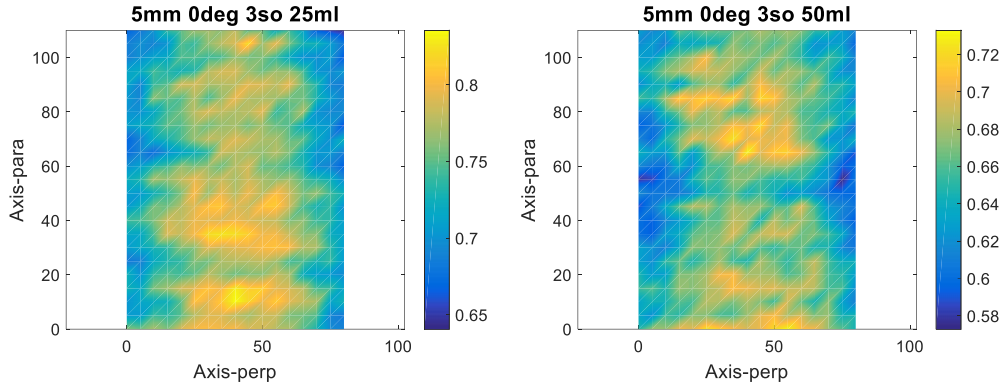


Figure 49. Difference in material loss between 25% (left) and 50% (right) material removal with a 3-in. standoff distance

In Figure 50 and Figure 51, a 10° tilt was shown to be detectable with the MFL system. However, the amplitude of the signal seems to weaken with a greater degree of tilt.

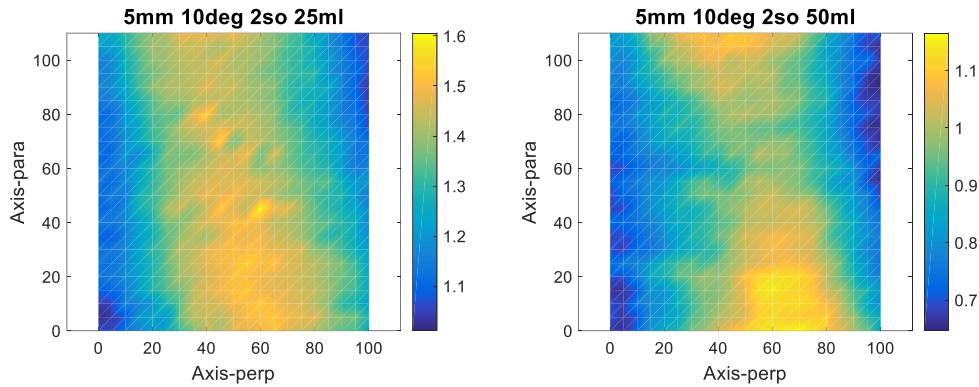


Figure 50. A 10° tilt combined with a standoff of 2 in., and material removal of 25% (left) and 50% (right)

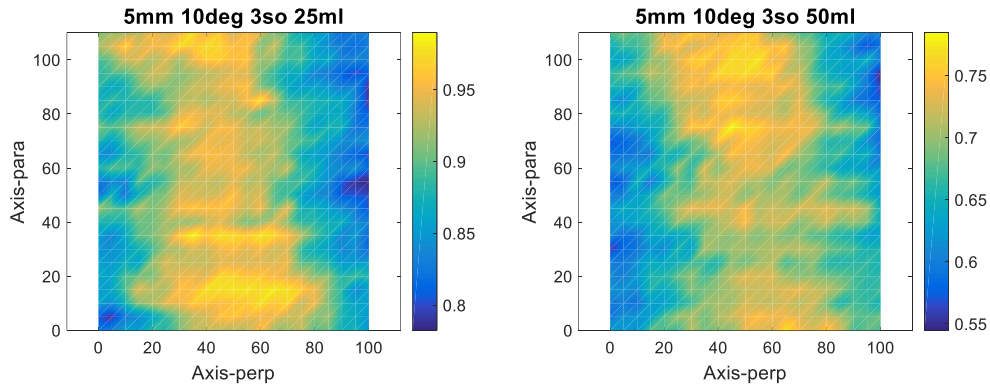


Figure 51. A 10° tilt combined with a standoff of 3 in., and material removal of 25% (left) and 50% (right)

When looking at an increase in the step increment of a scanning parameter, it was shown that an increase in the step increment in the Z direction of 5 mm seems to have a greater effect on the data collected as opposed to an increase in step in the X direction of 5 mm. This is illustrated in Figures 52 and 53.

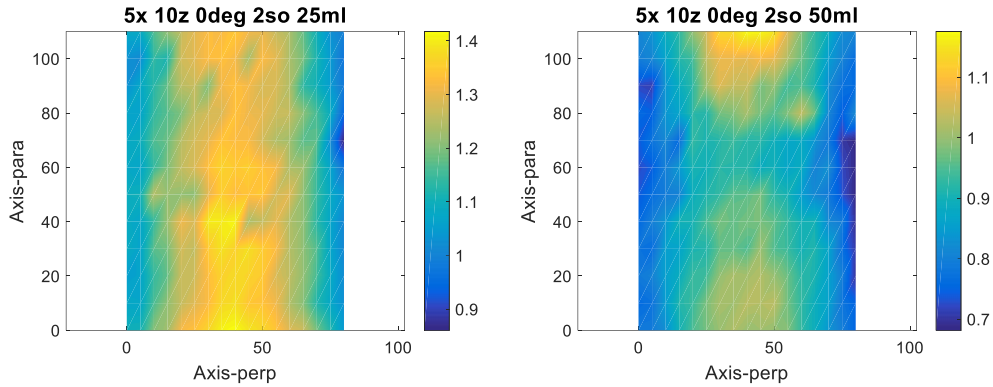


Figure 52. An increase of 5 mm in the Z direction during scanning, and material removal of 25% (left) and 50% (right)

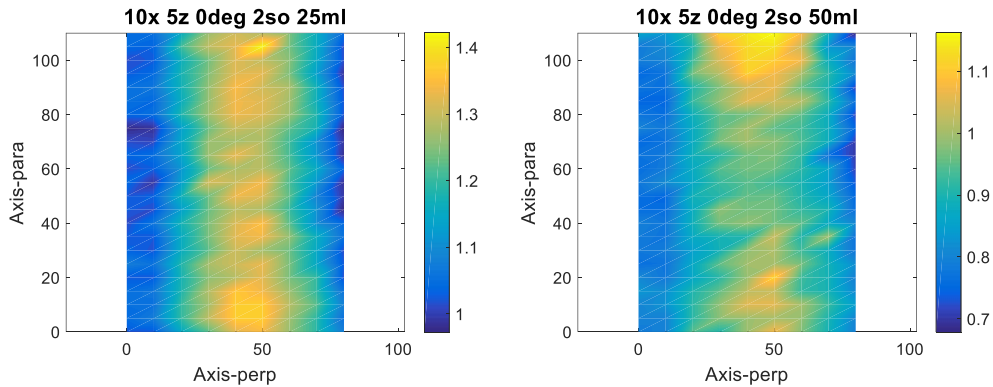


Figure 53. An increase of 5 mm in step in the X direction during scanning, and material removal of 25% (left) and 50% (right)

With a doubling of the step in both directions, an amount of material loss is still detectable. Figure 54 shows that in the reinforcing steel with a material loss of 50%, the amount of loss material is still detectable. In the 25% material loss (Figure 54, left), the material loss is not as noticeable.

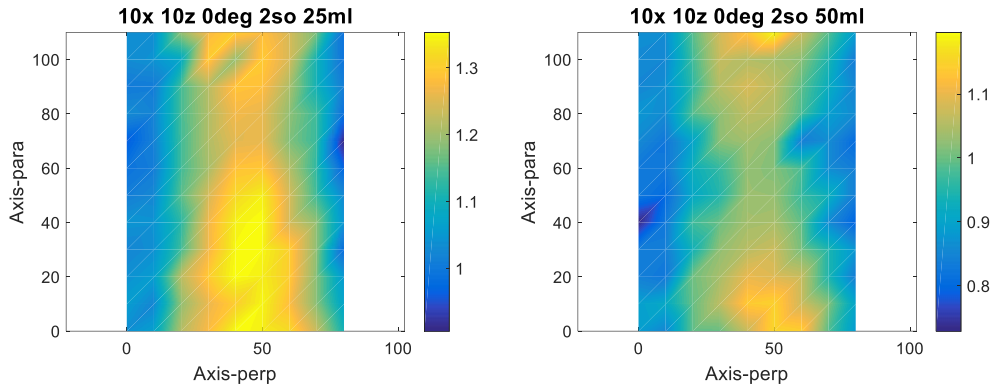


Figure 54. An increased step with 25% material loss (left) and an increased step with 50% material loss (right)

However, as can be seen in Figure 55, a change in tilt, along with an increase in step in both the X and Z directions, makes it increasingly difficult to determine material loss. In Figure 55a, the amount of material loss is almost undetectable.

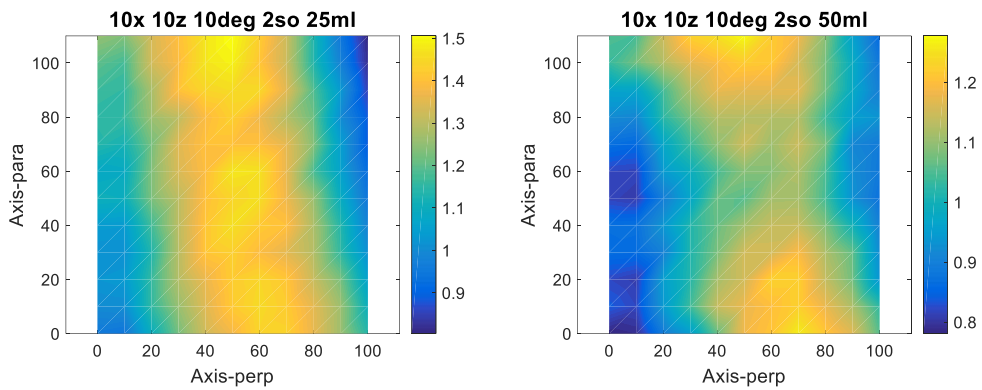


Figure 55. A change in step and in tilt angle for 25% material loss (left) and 50% material loss (right)

Measurements of MFL with Reinforcing Steel in Concrete Samples

The measurements made with the laboratory concrete samples were done with a standoff distance of 3 in. due to the required spacing of the reinforcing steel within the concrete samples. Based on the tests performed with the open reinforcing steel, only measurements of step increase and tilt were explored. Initial reaction to the test results indicated that material loss was more difficult to detect in the reinforcing steel surrounded by concrete. In looking at Figure 56 and Figure 57, it was clear that the amount of material loss was difficult to detect, while the tilt of the reinforcing steel was somewhat noticeable. From this example, it was decided to examine the amount of step in the X direction while keeping the step increment in the Z direction to 5 mm.

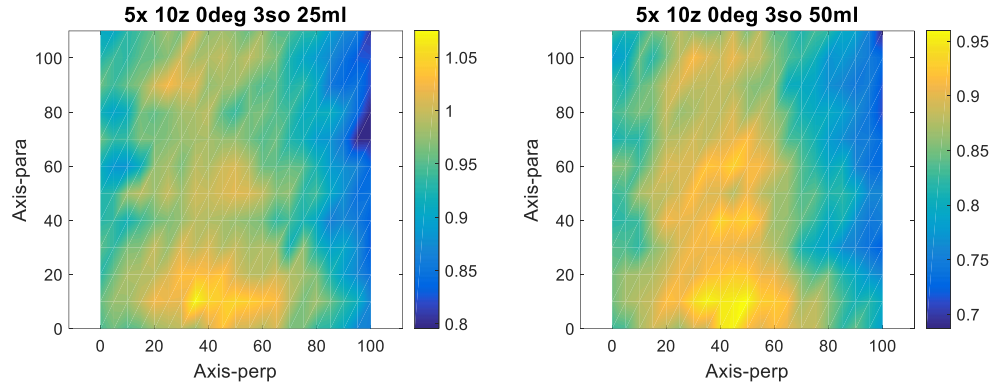


Figure 56. Concrete sample with a step increase in the Z direction with 0° tilt, and material removal of 25% (left) and 50% (right)

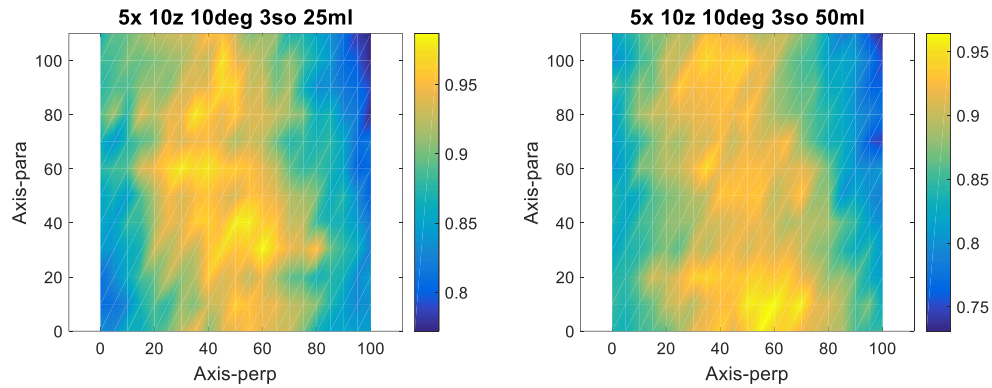


Figure 57. Concrete sample with a step increase in the Z direction with 10° tilt, and material removal of 25% (left) and 50% (right)

With the step increase in the X direction increased to 10 mm, while keeping the step increase in the Z direction to 5 mm, it can be seen that a better result was obtained by keeping the incremental distance for each measurement in the Z direction to a smaller value. By doing this, it can be easier to determine if there is a material loss, without regard to the slight tilt, and the result can be seen in comparing Figure 58 and Figure 59.

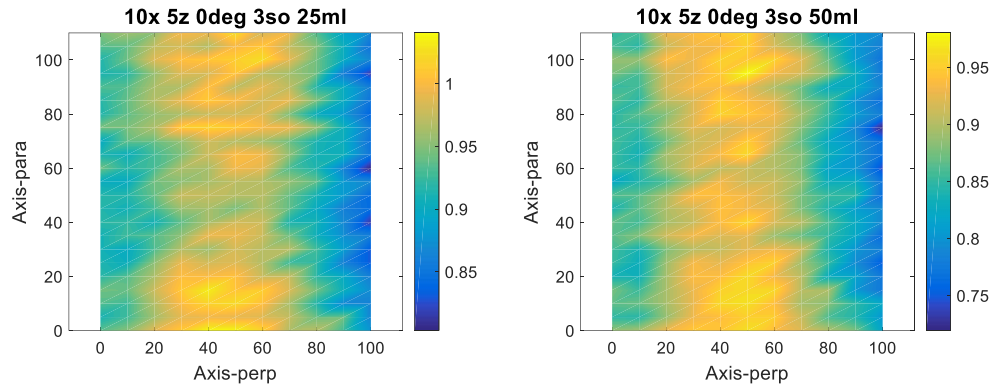


Figure 58. Concrete sample with a step increase in the X direction with 0° tilt, and material removal of 25% (left) and 50% (right)

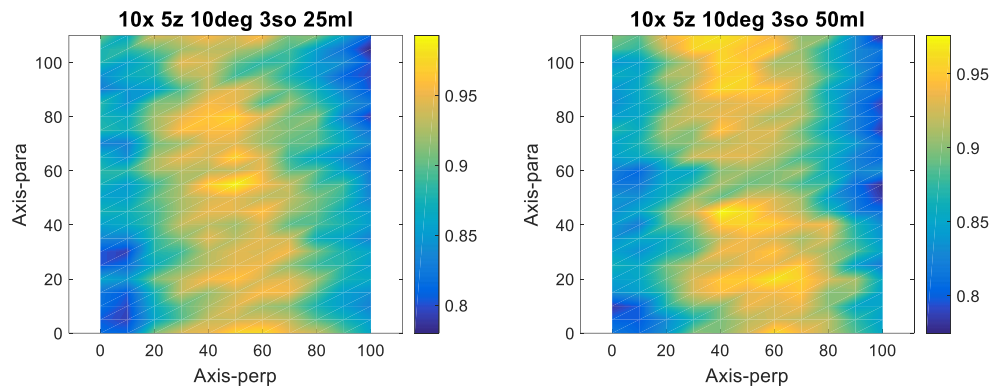


Figure 59. Concrete sample with a step increase in the Z direction with 10° tilt, and material removal of 25% (left) and 50% (right)

As a last measurement of scanning factors, and as a means to decrease the time required for each measurement scan, the step increment for both the X and Z directions was increased to 10 mm. From examination of the images in Figure 60 and Figure 61, it was difficult to determine the material loss for the 25% sample, left figure, while the 50% sample, right figure, did show a certain amount of material loss.

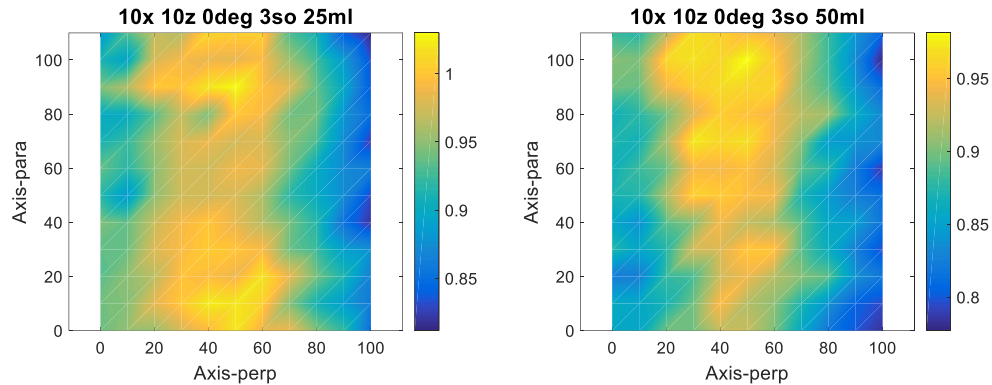


Figure 60. A 10 mm step for the X and Z directions with 0° tilt for material removal of 25% (left) and 50% (right)

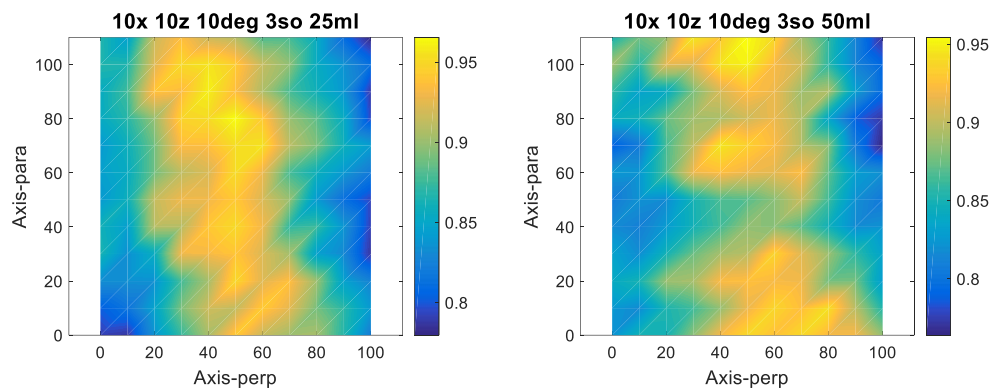


Figure 61. A 10 mm step for the X and Z directions with 10° tilt for material removal of 25% (left) and 50% (right)

During the laboratory work period of the research, it became evident that the system constructed for the MLF phase was not as reliable as that used in the initial phase of this type of research. This system was a pieced together system of various items of equipment, as opposed to the “off the shelf” system used in the GPR portion of the research. For this reason, there were times when the system would become unresponsive and malfunction in the laboratory. Despite this misbehavior, encouraging results were obtained in the laboratory, which led to the decision to take the system to the field for evaluation under more difficult conditions. Below are some summary points observed from the laboratory work.

Summary Points of MFL Laboratory Work

- Differences in material loss are detectable between 25% and 50% material removal.
- Tilt of the reinforcing steel does not seem to have as detrimental an effect on the detectability of material loss as does the increase in standoff distance.
- An increase in standoff distance from 2 in. to 3 in. makes detection of slight material loss (25%) more difficult to detect visually but greater material loss (50%) can still be detected visually.

- In concrete laboratory samples, an indexing spacing of 10 mm in both the X and the Z directions appeared to provide confidence in the detectability of material loss at 50% or greater.

Electromagnetic Bridge Results

Results from the bridge data collection were not as revealing as the laboratory data. Several factors inhibited the EM data collection, chiefly the condition of the bridge on the day of collection. Time was also a factor with only a limited amount of time available. After the GPR data collection, there was very little time to collect additional data. Finally, once the time for EM data collection was available, the equipment quit operating. The EM equipment was very sensitive to environmental conditions, and variations in outdoor conditions can affect the performance of the test setup. The equipment was not an “off-the-shelf” model, but was assembled specifically for this task. Another factor contributing to the difficult EM aspects of the project was that the individual responsible for Phase I of the project had left the university; therefore, other attempts were made to replicate the system used in Phase I. As shown in the previous section, the laboratory results were promising, and therefore, it was felt that data collection in the field might be possible, but unfortunately were not conclusive.

CONCLUSIONS AND RECOMMENDATIONS

In this project, the researchers worked to apply ultrasonic testing attenuation-measurement techniques to ground-penetrating radar. The field use of commercial GPR equipment (without auxiliary horns or other waveguides attached to the antennas) was easily carried out. Early results were promising, but more work is needed to explore error sources and the accuracy of the approximations being used. Spurious echoes arise easily due to the broad radiation patterns of the antennas and the finite size of concrete laboratory specimens. More work is required to locate optimal inspection setups where spurious signals are limited (or can be measured and subtracted), but key echoes remain readily observable. So far, there have been neglected signals resulting from reverberations within the air layers or concrete blocks. Modeling efforts that incorporate such signals must be explored. The researchers eventually hope to be able to make routine attenuation measurements in the field; for example, deducing concrete attenuation-versus-frequency curves from back wall echoes or reinforcing steel echoes. That capability will allow researchers to track attenuation changes over time as a possible indicator of concrete aging and deterioration in civil structures.

The effects of geometric variables on the GPR signal reflected from reinforcing steel bars were also investigated. Those variables included the distance from the antenna housing to the reinforcing steel, the orientation of the reinforcing steel relative to antenna housing axes, and the length and position of a reinforcing steel gap (representing metal loss due to corrosion). Measurements from the project indicate that GPR signal amplitude is quite sensitive to material loss, and care must be taken to compensate for those effects due to reinforcing steel depth and orientation. In addition, it is suggested to avoid working in regimes where wave interference effects can skew the amplitudes of reinforcing steel signals. For example, introducing a 1-in. gap into a long straight reinforcing steel bar can cause the signal reflected from the reinforcing steel to either rise or fall depending on the location of the gap relative to the antenna housing.

The use of a MFL system to detect the loss of material in reinforcing steel is feasible, but caution must be exercised in the use of this method, given the sensitivity of the system to outside influences. With the use of a generated magnetic field in a ferrous material, any surrounding metal capable of creating a magnetic field can interfere with the detection of material loss. Additionally, there is currently no commercially available system equipped to measure material loss. This makes the use of a laboratory system like the one used for this research difficult, and the system is susceptible to fluctuations in the voltage and current that power the many components needed to create the system. During laboratory testing, information on detection between 25% and 50% material loss, inspection step indexes, distance from the GMR sensors, and tilt of the steel was collected. It was determined that the horizontal speed of the sensor was not as sensitive as the indexing rate in the vertical direction, where differences in material condition can vary. The tilt of the steel is detectable, however, and the greater the degree of tilt that exists, the more difficult it would be to determine material loss. With the reinforcing steel embedded in concrete, the greater the amount of material loss is easier to detect, such that the 50% bars are easier to detect than the 25% bars. Although this method shows great potential, and good correlation between MFL and GPR existed in the earlier phase of this research, further research and development of a more environmentally sturdy piece of equipment is needed before this method of inspection can be widely used.

FUTURE WORK

Although the results of this phase of the research were not as promising as was anticipated at the beginning of the project, there is still potential for further research to be performed. It is suggested that a short research venture be done to evaluate the results of the GPR portion of the project. If there were a barrier rail slated for repair, a short-term project could be performed to take measurements prior to repair, measurements of the exposed reinforcing steel, and of the repair made to the barrier rail.

Once a full validation of the potential for GPR testing in measuring material loss of reinforcing steel is available, a GPR unit could be modified to provide more instantaneous feedback on the condition of the steel's material loss. This type of system could be used to decrease the time needed to decide whether to repair or replace existing barrier rails.

REFERENCES

- Eisenmann, D., F. J. Margetan, C.-P. Chiou, R. Roberts, and S. Wendt. 2013. Ground Penetrating Radar Applied to Rebar Corrosion Inspection. In *Proceedings of the 39th Annual Review of Progress in Quantitative Nondestructive Evaluation*. Vol. 32, pp. 1341–1348.
- Eisenmann, D., F. J. Margetan, C.-P. Chiou, R. Roberts, and S. Wendt. 2014. Progress in Quantitative GPR Development at CNDE. In *Proceedings of the 40th Annual Review of Progress in Quantitative Nondestructive Evaluation*. Vol. 33, pp. 1552–1559.
- Eisenmann, D., F. J. Margetan, and B. Pavel. 2015. GPR Measurements of Attenuation in Concrete. In *41st Annual Review of Progress in Quantitative Nondestructive Evaluation*. Vol. 34, pp. 114–121.
- Eisenmann, D., F. J. Margetan, L. Koester, and D. Clayton. 2016. Inspection of a Large Concrete Block Containing Embedded Defects Using Ground Penetrating Radar. In *Proceedings of the 42nd Annual Review of Progress in Quantitative Nondestructive Evaluation: Incorporating the 6th European-American Workshop on Reliability of NDE*. Vol. 35, pp. 020014-1–020014-10.
- Eisenmann, D., F. J. Margetan, C.-P. Chiou, S. Ellis, T. Huang, and J. Y. Tan. 2017. Effects of Position, Orientation, and Metal Loss on GPR Signals from Structural Rebar. In *43rd Annual Review of Progress in Quantitative Nondestructive Evaluation*. Vol. 36, pp. 080005–080005-10.
- Eisenmann, D., F. J. Margetan, and S. Ellis. 2018. On the Use of Ground Penetrating Radar to Detect Rebar Corrosion in Concrete Structures. In *44th Annual Review of Progress in Quantitative Nondestructive Evaluation*. Vol. 37, pp. 030009-1–030009-8.
- Jensen, T., S. Wendt, J. Gray, D. Eisenmann, F. Margetan, C. Lo, N. Nakagawa, and L. Brasche. 2013. *Feasibility Study for Detection and Quantification of Corrosion in Bridge Barrier Rails*. Institute for Transportation, Iowa State University, Ames, IA.
- Lai, W. L., T. Kind, and H. Wiggemhauser. 2010. A Study of Concrete Hydration and Dielectric Relaxation Mechanism Using Ground Penetrating Radar and Short-Time Fourier Transform. *EURASIP Journal on Advances in Signal Processing*, Vol. 2010, pp. 1–14.

**THE INSTITUTE FOR TRANSPORTATION IS THE FOCAL POINT FOR TRANSPORTATION
AT IOWA STATE UNIVERSITY.**

InTrans centers and programs perform transportation research and provide technology transfer services for government agencies and private companies;

InTrans manages its own education program for transportation students and provides K-12 resources; and

InTrans conducts local, regional, and national transportation services and continuing education programs.



**IOWA STATE
UNIVERSITY**

Visit www.InTrans.iastate.edu for color pdfs of this and other research reports.